

3D projection electrophoresis for single-cell immunoblotting

Samantha M. Grist ¹, Andoni P. Mourdoukoutas^{1,2} & Amy E. Herr ^{1,2,3}✉

Immunoassays and mass spectrometry are powerful single-cell protein analysis tools; however, interfacing and throughput bottlenecks remain. Here, we introduce three-dimensional single-cell immunoblots to detect both cytosolic and nuclear proteins. The 3D microfluidic device is a photoactive polyacrylamide gel with a microwell array-patterned face (xy) for cell isolation and lysis. Single-cell lysate in each microwell is “electrophoretically projected” into the 3rd dimension (z -axis), separated by size, and photo-captured in the gel for immunoprobng and confocal/light-sheet imaging. Design and analysis are informed by the physics of 3D diffusion. Electrophoresis throughput is >2.5 cells/s ($70\times$ faster than published serial sampling), with 25 immunoblots/ mm^2 device area ($>10\times$ increase over previous immunoblots). The 3D microdevice design synchronizes analyses of hundreds of cells, compared to status quo serial analyses that impart hours-long delay between the first and last cells. Here, we introduce projection electrophoresis to augment the heavily genomic and transcriptomic single-cell atlases with protein-level profiling.

¹Department of Bioengineering, University of California, Berkeley, USA. ²UC Berkeley – UCSF Graduate Program in Bioengineering, Berkeley, USA. ³Chan Zuckerberg Biohub, San Francisco, CA, USA. ✉email: ah@berkeley.edu

Proteins are biomolecules that play a direct role in nearly all cellular processes¹. As such, protein expression is a primary metric for quantifying cell state². Although genomics and transcriptomics analysis of gene and RNA expression are powerful and complementary measurement techniques, they often do not predict protein expression at the single-cell level^{3–5}. Proteoforms, or different forms of proteins arising from the same gene⁶, are also critical to understanding cell state: cellular heterogeneity at the proteoform level plays critical roles in cellular processes including regulating tumor growth⁷ and resistance to treatment in cancer⁸. Many single-cell proteomic technologies are limited to protein detection by antibodies with limited protein specificity, which may not be proteoform-specific⁹ and thus cannot distinguish proteoform-level heterogeneity. Protein separations based on electrophoresis can overcome these antibody specificity limitations through dual measurements of the physicochemical properties of protein targets (i.e., molecular mass, isoelectric point) and primary antibody reactivity for protein detection.

To offer a comprehensive understanding of complex cellular systems, selective detection of protein targets in individual cells is required; yet, key single-cell analysis challenges persist in throughput, sample preparation, and interfacing¹⁰. Measurement throughput is crucial to detect rare but important subpopulations of cells (e.g., metastasis, resistance to treatment), but—to attain suitable statistical power—the minimum sample size increases as subpopulation prevalence decreases¹¹. Thus, the ability to assay hundreds or even thousands of cells is valuable. Further compounding the challenge of measuring a large cell population with single-cell resolution is synchronously assaying all of the single cells. Proteomic cell state is dynamic¹² so differences in analysis time across cells can add artefactual heterogeneity—particularly when assessing cell response to drugs or environmental stimuli. Furthermore, single-cell lysate preparation and interfacing for interrogation must also preserve detectable protein concentrations from low single-cell copy numbers. Dilution into larger-than-a-cell volumes, sample losses, and lysate changes during transfer to an analysis platform can further challenge single-cell proteoform measurement¹⁰.

Since the early 1990s, capillary electrophoresis (CE) has been applied to surmount challenges in the analysis of lysate from individual cells¹³. To maintain protein target concentrations during analysis, CE uses fused silica capillaries with micron-scale diameters, facilitating efficient dissipation of Joule heating and ultra-rapid electrophoresis. For lysate transfer, the CE systems use the physical alignment of the capillary to reagent baths or isolated single cells. Early single-cell CE technologies were capable of assaying 10s of cells per day, making measurement of single-cell heterogeneity among large cell populations out of reach^{10,14}. CE improvements use capillary arrays for simultaneous analyses of samples¹⁵ and bundled 168-plex microstructured silica fibers (demonstrated to improve heat transfer rather than throughput)¹⁶. Analyte loss via adsorption to the capillary surface (due to large surface-area-to-volume ratios) challenges single-cell CE measurements¹⁰.

To advance single-cell resolution analyses, researchers brought both automation and microfluidic design to bear to efficiently integrate disparate sample preparation and electrophoretic analysis. In an excellent example, the Allbritton group introduced an automated, serial single-cell electrophoresis system by integrating a single glass capillary with a microwell array for cell isolation, using a motorized stage for microwell alignment to the capillary for serial sampling and analysis¹⁷. For analysis of a population of 219 mammalian cells, throughput was clocked at 2.1 cells/min (cell lysis, electrophoresis, and real-time fluorescence detection of sphingosine fluorescein and sphingosine-1-phosphate fluorescein). Also exemplar of integrated approaches, planar microfluidic devices support analysis of up to 12 cells/min^{18,19}. While useful, serial analysis of

large cell populations is inherently asynchronous and, as mentioned, can introduce artefactual cell-to-cell heterogeneity, particularly critical to assessing response to stimuli.

Mass spectrometry is a powerful, complementary separations technology that is promising for single-cell protein detection. Aside from mass cytometry²⁰, other forms of mass spectrometry do not rely on antibody specificity for selective protein detection. Highly multiplexed protein detection from single cells (1000s of targets per cell) is possible with bottom-up mass spectrometry, although throughput has not yet exceeded 100 individual cells^{21,22}. Mass spectrometry is limited to highly abundant proteins (>10⁴ copies per cell)^{21,22} and small-to-intermediate molecular masses for top-down proteomics (e.g., typically 25 kDa for MALDI-TOF, although specialized detectors facilitate detection of proteins up to 110 kDa^{23,24}). Furthermore, the vast majority of single-cell mass spectrometry approaches are bottom-up, wherein the requirement for protein digestion to peptides confounds proteoform stoichiometry. While top-down mass spectrometry does measure intact proteins—making the approaches relevant to proteoforms—and imaging mass spectrometry can assay larger numbers of cells (e.g., >1000 dorsal root ganglia)²⁵, larger proteins present a measurement challenge even with optimization for wider-range mass measurement (m/z 400 to 20,000)²⁵.

Immunoblotting is a class of separations with a powerful capacity for targeted proteomics. To detect protein targets a priori identified through hypotheses or discovery tools, this suite of separations approaches integrate two analytical modalities to yield enhanced target specificity over either alone: separation of proteins by electrophoresis and probing of specific targets by immunoreagents. While only recently developed for single-cell and sub-cellular resolution by our group, immunoblotting (and its most popular form, western blotting^{26,27}) has been a workhorse in biological and clinical laboratories for decades. Using automation in a different way to advance towards both single-cell resolution and multiplexed detection, the Kennedy group designed an automated system that integrates microchip electrophoresis with immunoprobation on an off-chip PVDF membrane²⁸. Integration between the microchip and membrane uses a mobile membrane, with the separations effluent deposited (blotted) onto that moving membrane. While not demonstrated for single-cell analysis, multiplexing was boosted to 11 separated protein targets from 9 serial separations in 8 min, with each separation from the same aliquot of bulk cell lysate with a total protein content similar to that of a single cell (400 ng total protein). Taking a different approach inspired by single-cell DNA electrophoresis (COMET assays)²⁹, we introduced single-cell western blotting with a throughput of ~200 cells/min³⁰. The planar 2D device uses a thin layer of polyacrylamide gel stippled with microwells for parallel cell isolation and lysis. Protein lysate is subjected to immunoblotting in the photoactive polyacrylamide gel abutting each microwell. We have applied the single-cell western blotting technology to studying heterogeneity of circulating tumor cells³¹, smooth muscle cells³², and HER2 isoform expression in clinical specimens³³. Furthermore, using similar design principles we have introduced single-cell immunoblotting tools based upon other physicochemical protein properties (e.g., subcellular localization³⁴ and isoelectric point^{35,36}) and adapted the single-cell western blot to assess adherent cells (without detachment)³⁷ and study invasive motility³⁸. These tools have emerged as powerful technologies for single-cell analysis; however, their throughput and sample consumption remain limited by the large spacing between microwells required for the protein separation axis.

Here, we introduce a high-density parallelized single-cell immunoblotting device that uses the third dimension (z -axis), to enhance the microwell array density and, hence, throughput

and sample consumption. In projection electrophoresis, we sought to leverage the full gel volume to map protein size and originating cell position from the 3D location of separated protein bands. The 3D design is inspired by multifunctional 3D hydrogel materials like Expansion Microscopy³⁹ and CLARITY⁴⁰, as well as the efficient electrotransfer of protein from gel to PVDF membrane in conventional western blotting^{27,41} and bulk separations in 3D and layered systems^{42–44}. Using a 3D volume improves microwell array density to 25 microwells/mm² from 2 microwells/mm² in 2D (planar) devices. Owing to this density improvement, the assay consumes an order of magnitude less volume of a cell suspension (25 μ L vs. 300 μ L) to assay ~300 cells (similar to planar systems), resulting in a 10-fold improvement in sample consumption. In this work, we describe the separation performance and use the physics of 3D diffusion to design the projection electrophoresis system, and perform near-simultaneous immunoblotting of both cytoplasmic (GAPDH, actinin, β -tubulin) and nuclear (PTBP1) protein targets from hundreds of single mammalian breast and brain tumor cells.

Results

Establishing projection electrophoresis as an analytical tool. In lieu of serial interrogation and electrophoretic analysis of individual mammalian cells, projection electrophoresis (Fig. 1a) yields synchronous, concurrent analyses of hundreds of single cells. Compared to serial-cell measurements, the parallel approach reduces assay-induced protein expression heterogeneity (Fig. 1b). After in-gel immunoprobing for the protein targets glyceraldehyde 3-phosphate dehydrogenase (GAPDH, involved in glycolysis, transcription, and apoptosis) and polypyrimidine tract-binding protein 1 (PTBP1, RNA-binding protein involved in cellular processes including splicing), projection electrophoresis yields 3D data (with xy position describing the originating microwell, z -position describing protein size, Fig. 1c–g). Mean- z -direction migration distances were 199 ± 9 μ m for PTBP1 (57 kDa) and 346 ± 7 μ m for GAPDH (37 kDa). Furthermore, the multifunctional, micropatterned polyacrylamide gel (PAG) serves as the cell isolation device, lysis vessel, separation matrix, and protein capture scaffold. This multifunctional gel thus facilitates *in situ* lysis, electrophoresis, and blotting, mitigating losses incurred in sample transfer steps, while synchronous analysis and fast assay times yield high assay throughput and drastically reduced sampling delays between cells in a population.

We first sought to verify the separation mechanism governing protein electrophoresis in the concurrent analyses (Fig. 2a, b). To understand the protein separation mechanism, we assessed electromigration of a ladder of well-characterized protein standards (donkey immunoglobulin anti-mouse IgG, IgG: 150 kDa; bovine serum albumin, BSA: 66.5 kDa; ovalbumin, OVA: 42.7 kDa, each labeled with AlexaFluor® dyes). When the purified protein solution is pipetted on top of the gel block (gel block face stippled with microwells), the protein solution preferentially partitions into the microwells (versus the hydrogel), thus providing a convenient, well-controlled means for sample loading into each microwell sample injector. To minimize 3D diffusional spreading during PAGE, we designed an ultra-short separation axis (1 mm, defined by the gel block thickness) and rapid (<1 min) protein PAGE duration. Upon completion of PAGE, the multifunctional gel was toggled from the separation matrix to a protein capture scaffold using a 45-second exposure to UV illumination⁴⁵.

We observed (Fig. 2c) a log-linear relationship of electromigration with molecular mass, as expected in size-sieving gel electrophoresis⁴⁶. Further, in this unique format, we observed constant-velocity and size-dependent electromigration for the ladder and additional protein assayed (Fig. 2d; electrophoretic mobilities of OVA:

$3.3\text{--}3.7 \times 10^{-5}$ cm²/Vs; BSA: $2.5\text{--}2.9 \times 10^{-5}$ cm²/Vs; transferrin: $1.3\text{--}1.7 \times 10^{-5}$ cm²/Vs, lectin: $0.96\text{--}1.14 \times 10^{-5}$ cm²/Vs; IgG: $7.4\text{--}8.0 \times 10^{-6}$ cm²/Vs). Constant-velocity migration required mitigation of deleterious effects of electrolysis (i.e., buffer pH changes, bubble formation at the electrodes), which increased the R^2 of linear fits to the protein migration data from 0.87 ± 0.06 to 0.97 ± 0.03 for the three ladder protein species (Supplementary Figure 1). For BSA and OVA ladder species, both a protein monomer and dimer are resolvable, as expected in high-performance protein PAGE^{47–49}. Having established the separation mechanism, we next estimated the PAGE performance by assessing the separation resolution (R_s). For two ladder proteins (OVA, BSA) in a 1 mm-thick 10%T PAG volume (Fig. 2e), the R_s reached 1.0 within 20 s of PAGE, yielding fully resolved species.

Based on the dominant separation mechanism and rapid protein separation, analysis of the purified protein ladder solution suggests that projection electrophoresis is suitable for analytical-quality protein analysis. The high performance of the rapid microfluidic protein analysis described here is in contrast to another 3D system, designed for preparatory z -direction separation performance, as previously demonstrated for bulk samples using a multilayered gel to coarsely fractionate small proteins (14–77 kDa) from large proteins (20–343 kDa)⁴⁴. In terms of throughput, each purified protein projection electrophoresis gel (100 μ m microwell pitch) contains >4000 microwells, facilitating >4000 parallel (replicate) purified protein separations for a total active assay throughput of 44 separations per second (not including readout time). For comparison, capillary array electrophoresis of a single sample yields a throughput of 5 separations per second¹⁵.

Device design is informed by 3D diffusion of target proteins.

Given the open microfluidic design of the projection electrophoresis device that uses a microwell array to perform sample isolation and preparation, with an abutting gel volume that performs the analytical functions (protein PAGE, immunoblotting), we sought to understand physics-based factors that set the minimum acceptable microwell-to-microwell spacing (microwell pitch, Δ_{well}). The Δ_{well} , in turn, sets the maximum number of concurrent protein PAGE separations per projection electrophoresis device. As illustrated schematically in Fig. 3a, the Δ_{well} spacing is influenced by the length scale of diffusional band broadening (σ_{xy} , in the xy plane) during protein PAGE along the z -axis. As design guidelines, the throughput of each single-cell projection electrophoresis device (number of single cells assayed per device) will be a function of Δ_{well} (sets separation lane density) and overall usable device dimensions (Fig. 3b). As Δ_{well} depends linearly on σ_{xy} , the maximum lane density is inversely proportional to σ_{xy}^2 , as computed in Fig. 3c. Two design rules are plotted: at $\Delta_{\text{well}} > 4\sigma_{xy}$, we would estimate <5% protein overlap between neighboring lanes, while at the more conservative $\Delta_{\text{well}} > 6\sigma_{xy}$, we would estimate <0.3% protein overlap assuming Gaussian protein distributions.

During electromigration, protein peaks will diffuse in three dimensions, with diffusion along the z -axis determining separation resolution (R_s) and diffusion in xy determining the minimum Δ_{well} . Diffusional spreading of protein bands in all three dimensions depends on protein molecular mass, temperature, time, and gel density (pore size)^{50,51}. To assess the impact of protein diffusion on setting Δ_{well} , we assessed the well-characterized fluorescently labeled OVA/BSA/IgG protein ladder during protein PAGE in a 7%T gel projection electrophoresis device. For each time point analyzed by confocal imaging, we determined the z position of the maximum of the summed fluorescence intensity, for an xy region of interest surrounding

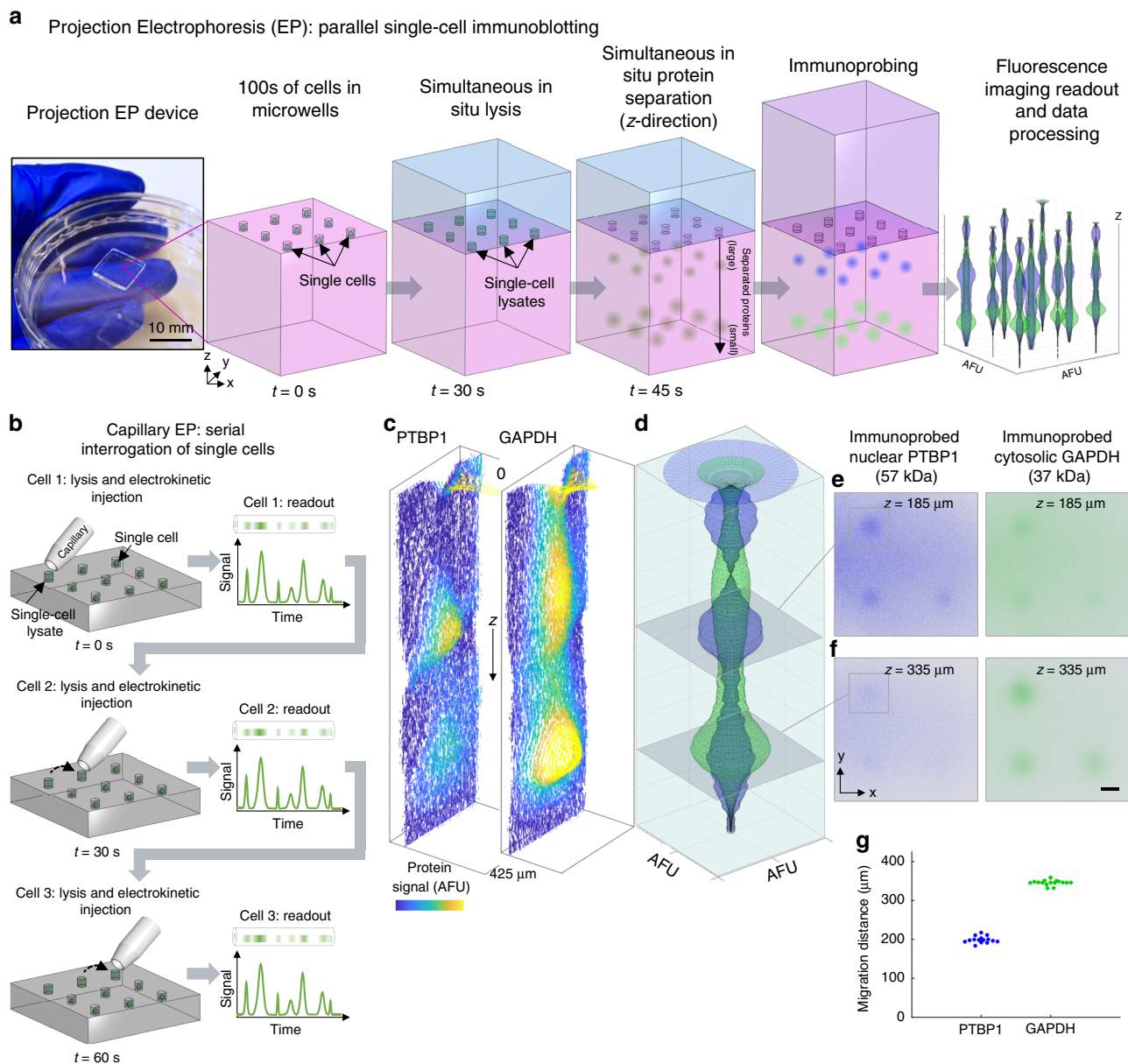


Fig. 1 Projection electrophoresis simultaneously lyses and separates both nuclear and cytosolic proteins from hundreds of single cells. **(a)** Projection electrophoresis device photograph and workflow schematic. A 9×9 mm projection electrophoresis PAG contains >1000 microwells that each serves as a separation lane. Cells in PAG microwells are lysed in situ using a lysis buffer-soaked hydrogel delivery matrix, and the lysate is then electrophoretically injected into the polyacrylamide and proteins are separated by size through the depth of the gel. After separation, proteins are covalently linked to the gel matrix using a UV-initiated capture. All cells are lysed and analyzed simultaneously, the active assay time (from cell lysis to photocapture) is less than 90 s, and in situ analysis reduces potential losses from transfer steps. **(b)** In contrast, capillary electrophoresis analyzes cells in series, with each cell lysed and proteins separated at a different time. **(c–f)** Different visualizations of z-directional protein separation in a single separation lane. **(c)** xz (y-summed) contour plots of background-subtracted protein signal within the separation lane for nuclear and cytosolic example proteins. Protein signal is visualized as peak height and false-colored. **(d)** z-directional intensity profiles (summed fluorescence intensity in arbitrary fluorescence units, AFU, vs. z) for PTBP1 (nuclear, blue) and GAPDH (cytosolic, green) in the same lane, revolved around the z -axis to generate a 3D rendering of fluorescence distribution. **(e, f)** Representative confocal xy slice images (representative of 9 confocal stacks acquired of different regions of 2 independent separation gels) for separated PTBP1 (blue) and GAPDH (green) at two z -depths into the gel (**e**) at the $185 \mu\text{m}$ depth of the PTBP1 band; (**f**) at the $335 \mu\text{m}$ depth of the GAPDH band). Each slice image shows 4 separation lanes, 3 of which appear to have been occupied by BT474 cells prior to analysis. Overlaid squares depict xy regions of interest for the lane plotted in **(c)** and **(d)**, over which fluorescence intensities were summed to yield z-directional intensity profiles. Scale bar represents $50 \mu\text{m}$. **(g)** Quantified z-migration distances for PTBP1 (57 kDa) and GAPDH (37 kDa) from $n = 15$ (PTBP1) and $n = 17$ (GAPDH) separation lanes. Source data are provided as a Source Data file.

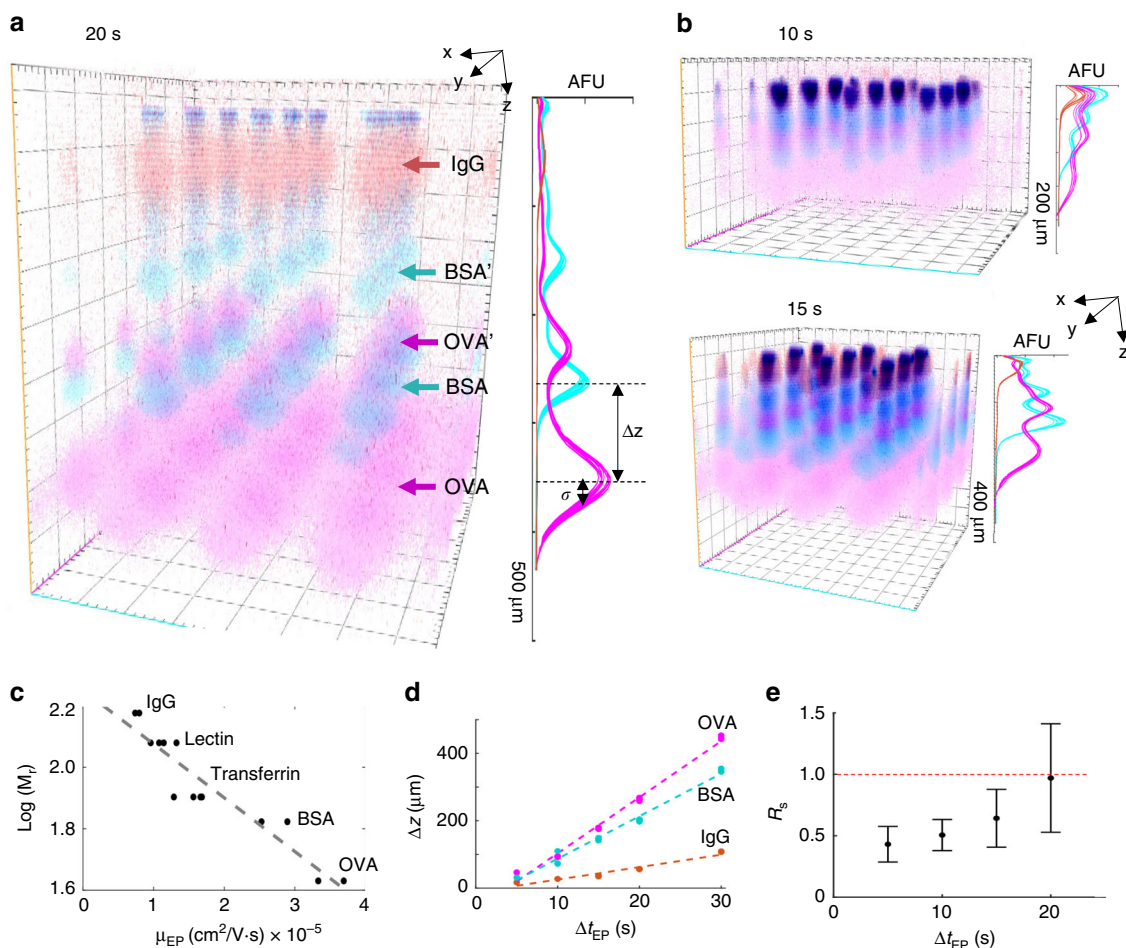


Fig. 2 Projection electrophoresis supports protein PAGE. (a) Confocal imaging of PAGE of fluorescently labeled protein ladder at 20 s elapsed separation time. Each ladder sample is injected from a 32 μm diameter microwell (xy plane) with PAGE along the z -axis of the gel block. Summing the background-subtracted fluorescence intensities at each pixel in the xy separation lane region of each slice image (a 300 pixel, 102 μm square region centered on each microwell) yields a z -intensity profile for each lane, with peak-to-peak displacement Δz and peak width σ (10%T PA separation gel containing 10% Rhinohide®). (b) 3D renderings and z -intensity profiles are plotted for (i) 10 s electrophoresis and (ii) 15 s electrophoresis in 10%T PAGs containing 10% Rhinohide® for comparison with the data for 20 s electrophoresis shown in (a). (c) The electrophoretic mobility of the proteins depends log-linearly on protein molecular mass. Each plotted point represents an electrophoretic mobility calculated from linearly fitting migration distance vs. electrophoresis time data from 11 to 17 segmented separation lanes in $n = 5$ 7%T PA separation gels containing 10% Rhinohide® (5 electrophoresis times). Linear fitting yields $\log(M_r) = 1.7 \times 10^4 \mu_{EP} + 2.25$ ($R^2 = 0.89$). (d) Electromigration distance depends linearly on electrophoresis time, thus proteins migrate at constant velocity during PAGE. Migration distances are plotted from protein bands originating from 11 to 17 nearby microwells in two independent 7%T PA gels containing 10% Rhinohide®; 33 mA constant current; 52 V/cm initial, 2 gels for each migration time. Linear fitting yields OVA migration = 16.7t-63.42; BSA migration = 12.64t-39.3; IgG migration = 3.69t-11.54. (e) Separation resolution, R_s , for BSA and OVA peaks in 10%T PAGE gels containing 10% Rhinohide®. Each point depicts the mean and standard deviation of the R_s calculation from the median migration distances and peak widths from $n = 4$ independent separation gels. Source data are provided as a Source Data file.

each microwell injector. At this z position, we assessed xy resolution by Gaussian fitting x and y intensity profiles and extracting the mean fitted peak width σ_{xy} . For duplicate gels of 5 electrophoresis times, we plotted the squared peak width vs. time in gel, fitting to the expected diffusional peak spreading⁵⁰:

$$\sigma_{xy}^2 = \sigma_{xy,0}^2 + 2Dt_{diff}. \quad (1)$$

For each protein target, σ_0 is related to the injected peak width (dictated by microwell diameter), D is the in-gel diffusion coefficient, and t is the total elapsed time since protein injection. Figure 3a shows an example confocal fluorescence data xy slice image for OVA and associated Δ_{well} design rule. Applying the analysis to the full protein ladder (Fig. 3d), yields estimates of Δ_{well} across a range of protein targets and diffusion coefficients ($D_{OVA} \sim 16 \mu\text{m}^2/\text{s}$, $D_{BSA} \sim 7 \mu\text{m}^2/\text{s}$, $D_{IgG} \sim 2.7 \mu\text{m}^2/\text{s}$ calculated

from linear fits to the plot of σ_{xy}^2 vs. diffusion time). Under the described conditions, the protein target with the largest D (OVA) suggests that a Δ_{well} of 200 μm will satisfy the trade-off of maximizing separation lane density while minimizing separation lane overlap (7%T gels, 10 s protein PAGE). For comparison, top-down MALDI imaging mass spectrometry utilizes a protein spot pitch of 20–200 μm ²⁴.

To further understand the diffusion-driven interdependency of the microwell spacing and separation performance, for the highest diffusivity ladder protein (OVA) we modeled the maximum assay time (the time at which protein signal is expected to bleed into the neighboring lane, from the diffusional peak spreading function above) for a range of microwell spacings (Fig. 3e), as well as the R_s as a function of electrophoresis time and electric field strength (Fig. 3f). The separation resolution R_s is

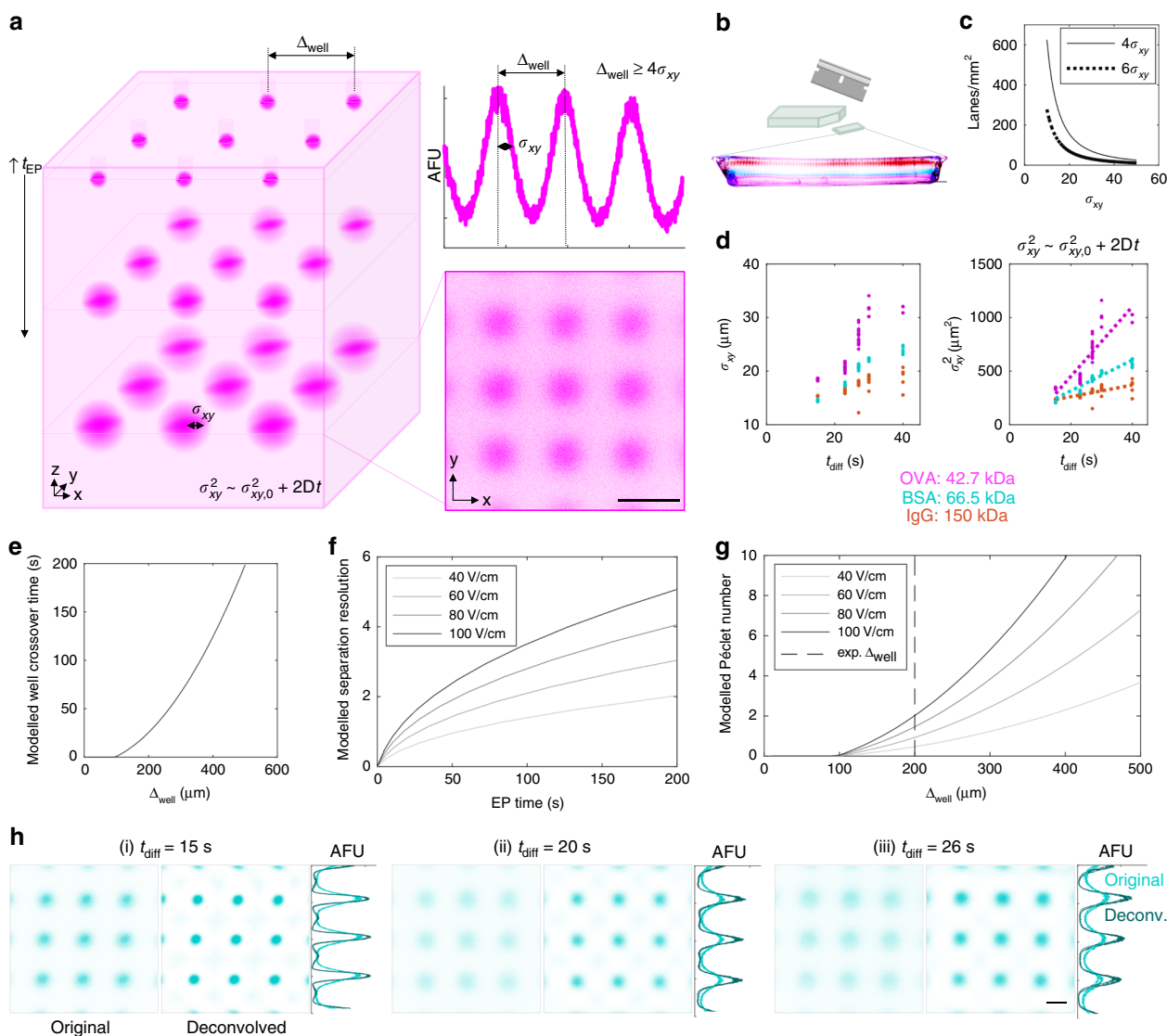


Fig. 3 The physics of 3D diffusion dictate projection electrophoresis device design and inform image analyses. (a) Lane density (limited by minimum spacing between separation lanes Δ_{well}) is dependent on separated protein xy bandwidth (σ_{xy}) to avoid microwell-microwell crosstalk. σ_{xy} in turn depends on 3D diffusion of the injected protein. Simulated data shown in the left schematic; measured OVA data shown in micrograph and intensity profile (representative of two independent separation gels). Scale bar represents $100 \mu\text{m}$. (b) Throughput is a function of both lane density and usable gel area; separated protein bands parallel to the gel edges in a cross-sectional image of the gel show uniform migration across the gel. Scale bar represents 1mm . (c) Theoretical maximum lane density at a spacing of $4\sigma_{xy}$ ($\sim 5\%$ overlap between lanes) and $6\sigma_{xy}$ ($\sim 0.3\%$ overlap between lanes). Maximum lane density is inversely proportional to σ_{xy}^2 . (d) Measured diffusional band broadening (Gaussian fit peak width σ_{xy}) from purified proteins initially partitioned into $32 \mu\text{m}$ microwells, as a function of in-gel diffusion time (t_{diff}). Left: σ_{xy} vs. t_{diff} . Right: σ_{xy}^2 vs. t_{diff} with linear fits ($\sigma_{xy}^2 = \sigma_{xy,0}^2 + 2Dt_{\text{diff}}$). After 10s EP, we measure $\sigma_{xy} < 30 \mu\text{m}$ for all proteins, suggesting that $200 \mu\text{m}$ microwell spacing is sufficient. Linear fitting yields OVA $\sigma_{xy}^2 = 32.5t_{\text{diff}} - 198$ ($R^2 = 0.75$); BSA $\sigma_{xy}^2 = 14.3t_{\text{diff}} + 29.8$ ($R^2 = 0.88$); IgG $\sigma_{xy}^2 = 5.41t_{\text{diff}} + 153$ ($R^2 = 0.42$). (e) Modeled time for ovalbumin bands to diffuse into the neighboring lane, as a function of microwell spacing Δ_{well} . (f) Modeled separation resolution for BSA and OVA, as a function of EP time and electric field strength. (g) Modeled Péclet number (defined as the ratio of the time to reach a BSA-OVA separation resolution of 1 to the time at which the OVA band is expected to diffuse into the neighboring separation lane). (h) Physics-driven postprocessing. For each confocal slice (BSA, 7%T gel), the original image, that after physics-driven postprocessing (deconvolution of a point spread function modeling 3D diffusion), and summed pre- and post-deconvolution intensity profiles for a $100 \mu\text{m}$ region surrounding each row of protein bands are shown. Each image pair is scaled to the maximum of the (higher-intensity) deconvolved image. Scale bar represents $50 \mu\text{m}$. Source data are provided as a Source Data file.

modeled as⁵²:

$$R_s = \frac{\Delta z}{\frac{1}{2}(4\sigma_1 + 4\sigma_2)} = \frac{\Delta\mu_{EP}Et}{\frac{1}{2}(4\sqrt{\sigma_0^2 + 2D_1t} + 4\sqrt{\sigma_0^2 + 2D_2t})}, \quad (2)$$

where Δz is the difference in migration distance between the two protein targets, σ_1 and σ_2 are the z -direction peak widths, $\Delta\mu_{EP}$ is the difference in electrophoretic mobility between the two targets, E

is the electric field, and D_1 and D_2 are the diffusion coefficients for the two targets. The diffusion coefficients for BSA and OVA ($D_{\text{BSA}} = 13.1 \mu\text{m}^2\text{s}^{-1}$, $D_{\text{OVA}} = 16.8 \mu\text{m}^2\text{s}^{-1}$) were estimated at $25 \text{ }^\circ\text{C}$ from the Stokes-Einstein equation⁵⁰ and adjusted for in-gel diffusion⁵¹ (7%T gel) as described in the Methods. The electrophoretic mobilities were empirically determined from the results of Fig. 2d ($\mu_{\text{BSA}} = 2500 \mu\text{m}^2\text{V}^{-1}\text{s}^{-1}$, $\mu_{\text{OVA}} = 3300 \mu\text{m}^2\text{V}^{-1}\text{s}^{-1}$). We next defined a Péclet number as the ratio of the maximum assay

time to the time required to reach $R_s = 1$, with results presented in Fig. 3g and the Péclet number given by:

$$Pe = \frac{t_{\text{band overlap}}}{t_{R_s=1}} = \frac{t_{\Delta_{\text{well}} = 6\sigma_{xy}}}{t_{R_s=1}}. \quad (3)$$

At $\Delta_{\text{well}} = 200 \mu\text{m}$ (Fig. 3d), $Pe \sim 1$ for an applied electric field strength of 60 V/cm. As protein band diffusion measurements (Fig. 3d) suggest measured diffusion coefficients smaller than predicted values, our Péclet analysis is a conservative estimate of the trade-off between separation performance and achievable microwell density. Separation resolution is proportional to electric field E , thus, increasing E increases the Péclet number. E is equal to the voltage drop divided by the distance over which the voltage is dissipated. If the distance between electrodes is increased (e.g., by placing separation lanes in series between the electrodes, as configured for 2D immunoblotting³⁰), higher driving voltages are required to reach the same E which can exceed power supply voltage limits. While we demonstrate electric fields of 43–68 V/cm in this work, future research regarding even higher E operating regimes (e.g., 100 V/cm using 30 V across 0.3 cm) would shed light on limitations arising from regime-relevant physics and chemistry (i.e., Joule heating, electrolysis). Joule heating and electrolysis both increase with electric current. Joule heating reduces separation resolution and introduces nonuniformities (via nonuniform heat dissipation)⁵². Electrolysis generates acid and base ions and creates bubbles that can modulate the electrophoretic mobility and disrupt the electric field⁵³ (e.g., pre-optimization projection electrophoresis system depicted in Supplementary Figure 1).

Building on an understanding of the dominant physics, namely diffusion, we next sought to investigate computational approaches to recover starting concentration distributions (here, the microwell array) from endpoint confocal fluorescence images of the protein PAGE (Fig. 3h). Recovery of starting protein concentration distributions will both enhance separation lane density, and facilitate future reconstruction of complex distributions such as those expected in adherent cells and tissue slices. In microscopy, deconvolution of an experimentally, theoretically, or computationally-determined, microscope-dependent point spread function (psf) recovers spatial resolution by image postprocessing^{54–56}. Inspired by deconvolution in microscopy, we explored whether we could represent the final protein projection image ($I(x, y, z, t)$) as the initial protein xy pattern ($p_0(x, y, z)$; related to the spatial arrangement of cells/microwells) convolved with a ‘diffusional point spread function’ $\text{psf}_{\text{diff}}(x, y, z, t)$, in turn, convolved with the imaging point spread function $\text{psf}_{\text{img}}(x, y, z, t)$:

$$I(x, y, z, t) = p_0(x, y, z) \otimes \text{psf}_{\text{diff}}(x, y, z, t) \otimes \text{psf}_{\text{img}}(x, y, z, t). \quad (4)$$

We chose to describe the diffusional psf_{diff} using 3D point-source diffusion⁵⁷:

$$\text{psf}_{\text{diff}}(x, y, z, t) = \frac{M}{(4\pi Dt)^{3/2}} \cdot \exp\left(-\left(\frac{x^2 + y^2 + z^2}{4Dt}\right)\right), \quad (5)$$

where D is again the protein diffusion coefficient, t the elapsed diffusion time, and M the starting number of molecules at the point source. Although we estimated the full 3D point spread function for each protein, we performed 2D deconvolution only on the individual slice images, without using information from neighboring focal planes (as in a “no-neighbors” deconvolution imaging method⁵⁸). We used this approach to simplify processing, while recognizing that the simplification limits a full 3D reconstruction and the signal intensity improvement possible from 3D deconvolution. To perform 2D processing, we deconvolved the 2D function psf_{diff} (through the center of the

point spread function, at $z = 0$) from 2D confocal slice images at the z -direction migration peak for each protein (the z position at which the summed intensity for that protein in the image field of view was maximized). We neglected the effects of psf_{img} , as we expect that the resolution of our measurement is more limited by diffusion (tens of microns for our typical time scales, as shown in Fig. 3a) than by the resolution of confocal microscopy with high NA objectives (typically sub-micron⁵⁹).

After deconvolution of the protein PAGE images, we observe a considerable improvement in spatial resolution of xy profiles of separated BSA (Fig. 3h; 5–15 s elapsed PAGE duration in (i)–(iii)). Comparing the “original” to the “deconvolved” images illustrates that spatial resolution is improved from $\sigma_{xy} = 16 \pm 2 \mu\text{m}$ to $\sigma_{xy} = 8.4 \pm 0.2 \mu\text{m}$ (47%) for 5 s electrophoresis (15 s total time until photocapture), $\sigma_{xy} = 25.7 \pm 0.6 \mu\text{m}$ to $\sigma_{xy} = 13.1 \pm 0.6 \mu\text{m}$ (49%) for 10 s electrophoresis (20 s total time), and $\sigma_{xy} = 26.3 \pm 0.6 \mu\text{m}$ to $\sigma_{xy} = 13.3 \pm 0.5 \mu\text{m}$ (49%) for 15 s electrophoresis (26 s total time). Further, the localization of the peak center was unperturbed by reconstruction ($\Delta\mu < 1.1 \mu\text{m}$ for all analyzed protein spots, with $\Delta\mu_{\text{avg}} = 0.38 \mu\text{m}$) and the integrated fluorescence signal of each protein sample is minimally perturbed by the reconstruction except when visible artefacts were present in the deconvolved images as shown in the lowest electrophoresis time (i) (average AUCs after postprocessing are within 3% of the initial values in (ii–iii), but 24% in (i)). Measured errors in peak center were $\Delta\mu = 0.08 \pm 0.06 \mu\text{m}$ ($t_{\text{diff}} = 15 \text{ s}$), $\Delta\mu = 0.68 \pm 0.3 \mu\text{m}$ ($t_{\text{diff}} = 20 \text{ s}$), $\Delta\mu = 0.1 \pm 0.2 \mu\text{m}$ ($t_{\text{diff}} = 26 \text{ s}$); measured errors in peak AUCs were $\Delta\text{AUC} = 23.9 \pm 1.4\%$ ($t_{\text{diff}} = 15 \text{ s}$), $\Delta\text{AUC} = 0.5 \pm 0.8\%$ ($t_{\text{diff}} = 20 \text{ s}$), $\Delta\text{AUC} = 3 \pm 2\%$ ($t_{\text{diff}} = 26 \text{ s}$) ($n = 9$ ROIs). Under ideal conditions, physics-based postprocessing is expected to report a time-invariant σ_{xy} . We do observe a weak dependence of σ_{xy} on time, which we attribute to estimated model parameters (including diffusion coefficient, in-gel temperature, hydrodynamic radius, gel density, and diffusion time) and depth-dependent imaging artefacts arising from refractive index mismatch between the separation gel and immersion medium (psf_{img} was neglected in our analysis). Future study will benefit from refinement of the model; however, the physics-based image postprocessing introduced here offers a means to reconstruct a map of the initial sample specimen from the target concentration distributions in the 3D gel volume, all based on the endpoint fluorescence readout of protein PAGE.

Sample preparation design for single-cell projection electrophoresis. Having considered the design of the projection electrophoresis device and assay using a well-characterized protein ladder, we next sought to identify factors important to high-performance protein PAGE of single cells (Fig. 4). We first assessed the settling of single BT474 cells in 25 μm diameter microwells within the projection electrophoresis gels. Figure 4a depicts settled Calcein-stained BT474 breast tumor cells in microwells after gravitational settling and convective wash-off of cells settled outside of microwells. A corresponding full-gel wide-field microscopy image of immunoprobed GAPDH fluorescence after the projection electrophoresis assay is also shown; probed protein bands correlate with settled cell positions. Cell settling efficiencies (populated microwells) were at $43 \pm 8\%$ with the number of settled single cells 356 ± 82 per $9 \times 9 \text{ mm}$ projection electrophoresis device ($n = 5$ devices). The fraction of microwells occupied by more than one cell was $10 \pm 3\%$. Further optimization of cell settling densities, microwell geometries, settling times, and wash parameters would likely improve these values and thus assay throughput.

After protein solubilization, diffusion-driven dilution of single-cell lysate occurs rapidly in the open microwell geometries. To

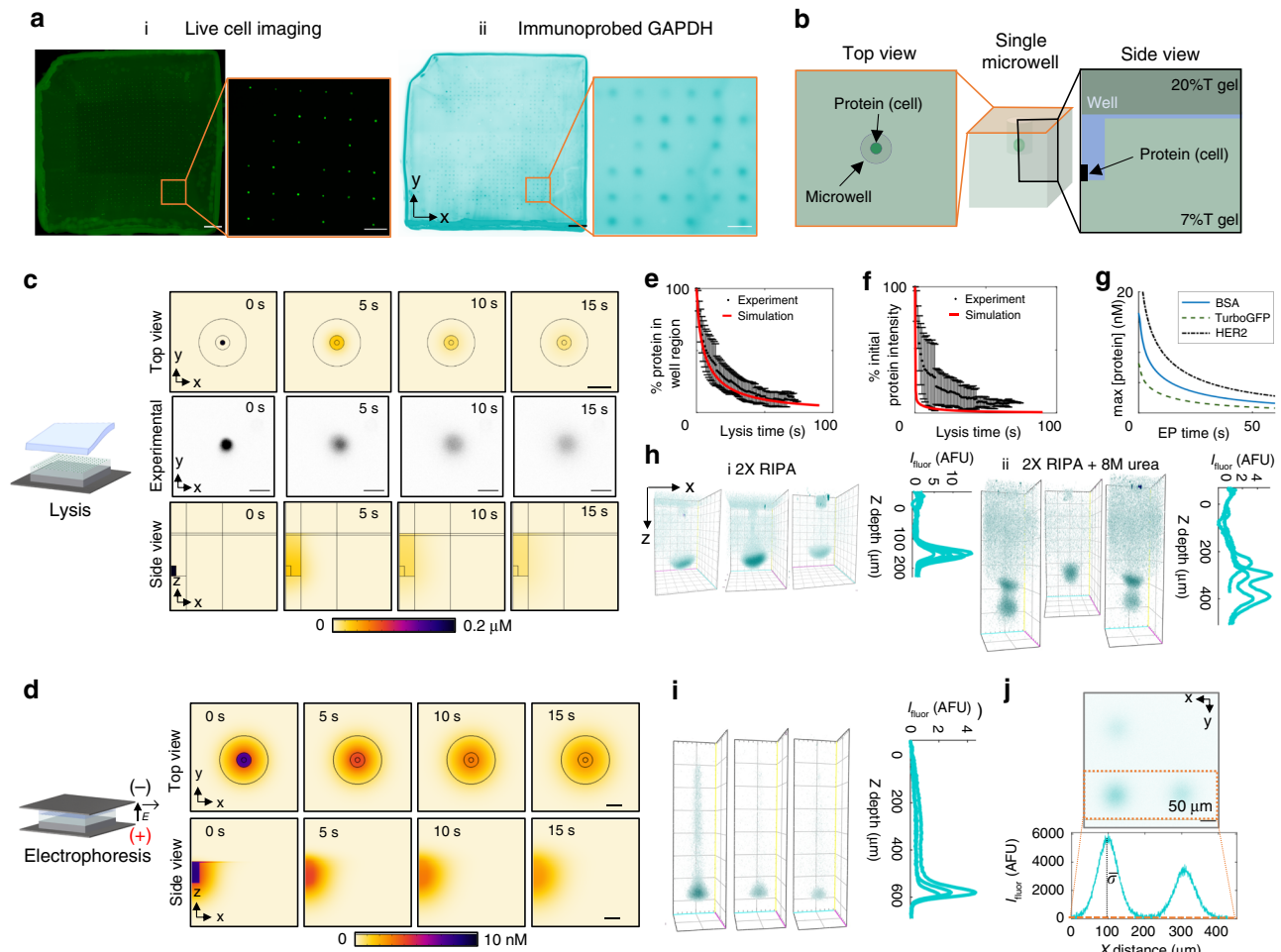


Fig. 4 Design and verification of sample preparation for projection electrophoresis of single mammalian cells. **(a)** High-density endogenous protein bands (ii) correspond to single-cell settling in microwells (i). Scale bars represent 1 mm (left full-gel images) and 200 μm (right zoom images). **(b)** Illustration of top-view and side-view geometries shown in protein dilution studies (**c**, **d**). **(c)** Modeling and experimental quantification of diffusional dilution during lysis. Simulated and experimental top-view images of diffusional protein dilution during lysis, and side-view simulated results are shown. The simulated initial TurboGFP concentration was 2 μM . Experimental image is representative of 12 monitored cells across 3 independent lysis experiments. Scale bars represent 50 μm . **(d)** Modeling the impact of diffusion during electrophoresis on detectable in-gel protein concentration. Side and top view TurboGFP concentration profiles are shown at different times during electrophoresis. Simulated initial TurboGFP concentration (before lysis and electrophoresis) was 2 μM . Scale bars represent 30 μm . **(e)** Quantification of the percent of protein remaining in the microwell region during lysis (experiment plots mean and standard deviation of $n = 12$ cells across 3 lysis experiments). **(f)** Quantification of the change in the spatial maximum protein concentration as a function of time after protein solubilization (experiment plots mean and standard deviation of $n = 12$ cells across 3 lysis experiments). **(g)** Simulated maximum protein concentration vs. electrophoresis time, for 3 model proteins. **(h)** Representative β -tubulin separations from U251 glioblastoma cells lysed with different buffer formulations (2 \times RIPA lysis buffer and 2 \times RIPA including 8 M urea), both after 10 s electrophoresis. Lysis/EP buffer requires 8 M urea for fast protein solubilization and electromigration. **(i)** Maximum intensity projection 3D renderings and z-intensity profiles of probed GAPDH bands from single BT474 breast tumor cells. **(j)** Microwell packing density (impacting assay throughput) is dependent on protein band diffusion before photocapture. Protein diffusion profiles confirm that a microwell pitch of 200 μm is sufficient to resolve bands from neighboring microwells. After 10 s EP, the mean peak width (σ_{xy}) of the xy GAPDH spots is $32 \pm 11 \mu\text{m}$ (mean \pm standard deviation of $n = 47$ single-cell separation lanes across 5 replicate separation gels). The depicted confocal slice micrograph is representative of 20 confocal image stacks, across different regions of 5 replicate separation gels. At a microwell pitch of 192 μm ($6\sigma_{xy}$), <0.3% of the signal should bleed into the neighboring lane. Scale bar represents 50 μm . Source data are provided as a Source Data file.

determine how the concentration of the single-cell protein lysate changes during the lysis and electrophoresis stages of the assay, we used a combination of finite-element modeling (geometries are shown in Fig. 4b) and experimental monitoring of TurboGFP-expressing U251 cells during cell lysis (Fig. 4c) and finite-element modeling during electrophoresis (Fig. 4d). To compare simulation and experiment, we integrated the 3D protein concentrations over the full z range of the model to mimic detected wide-field fluorescence intensities (Fig. 4e, f). Using this metric, after a typical 25 s lysis time, we measure $17\% \pm 11\%$ of the initial protein

intensity. Our simulated profiles overestimate the diffusional dilution of protein, predicting only 2.2% of the initial intensity for in-well lysis after 25 s. We attribute the $\sim 15\%$ discrepancy to delayed solubilization of cellular protein (the models assumed complete solubilization at $t = 0$), overestimates of the predicted diffusion coefficient used in the simulation, or a possible diffusion barrier on the microwell wall surface arising from either the presence of Rhinohide[®] in the gel matrix or the presence of residual Gelslick[®] or dichlorodimethylsilane used during gel fabrication. One important consideration for projection electrophoresis is

that while considerable in-gel protein dilution remains, in contrast to 2D single-cell immunoblots^{30,34,35}, there is reduced protein 'loss' from the gel in the projection electrophoresis platform. While other electrophoretic cytometry assays have a fluid layer or lid gel above the thin separation gel, into which protein can diffuse and is lost, in the projection electrophoresis device most (if not all) protein is mobilized into the bulk of the 3D gel when an electric field is applied to initiate PAGE.

We then sought to quantify how the maximum protein concentration changes during the analytical single-cell PAGE stage (Fig. 4g) using finite-element modeling. From an initial protein concentration of 2 μM in a cylinder representing the cell, we estimate maximum protein concentrations of 2.1 nM (TurboGFP, 26 kDa), 4.0 nM (BSA, 66.5 kDa), and 6.8 nM (HER2, 185 kDa) after 25 s lysis and 20 s electrophoresis in Fig. 4g. We compared the expected diffusional dilution during electrophoresis to that expected in a planar system (Supplementary Figure 2) and found similar dilution during the assay steps in both systems. We note that the planar system is amenable to imaging during electrophoresis, thus our comparison (which predicts similar losses to those reported in our previous work⁵²) serves as validation of the numerical model. Diffusional dilution of protein is dependent on both analyte size and gel density. The relatively large-pore-size gels used in this work (7%T) are optimal for large analytes (80–200 kDa), with adaptation for smaller analytes accommodated by moving to higher-density (smaller pore size) separation gels.

In optimizing the projection assay, we sought buffer chemistries to minimize lysis and solubilization times and used diffusive immunoprobings of model proteins β -tubulin and GAPDH using immunoglobulin fragments (F(ab) fragments) to assess solubilization efficacy. Here, we assessed a range of cell lysis and protein solubilization chemistries (Fig. 4h). Across a range of chemistries, we observed differences in protein electromigration and dispersion, which were dependent on buffer composition and delivery methods. We selected a dual-function lysis and solubilization buffer that utilizes the anionic detergents sodium dodecyl sulphate (SDS) and sodium deoxycholate, augmented with a strong chaotrope (8 M urea). Comparing solubilization, electromigration, and dispersion of the model protein β -tubulin from U251 glioblastoma cells lysed both without (i) and with (ii) 8 M urea in the lysis buffer, we observed rapid electromigration into the 3D gel from the microwell and lower protein peak dispersion with urea present. Without urea, the 3D protein bands exhibited a hollow, bowl-like shape (concave towards the microwell), rather than the 3D Gaussian distribution which would be expected from diffusion theory. In a sub-set of separation lanes, two β -tubulin peaks were detectable after solubilization with urea lysis buffer (Fig. 4h), suggesting delayed solubilization for a subset of the β -tubulin molecules, as might be expected depending on the intracellular state of the β -tubulin.

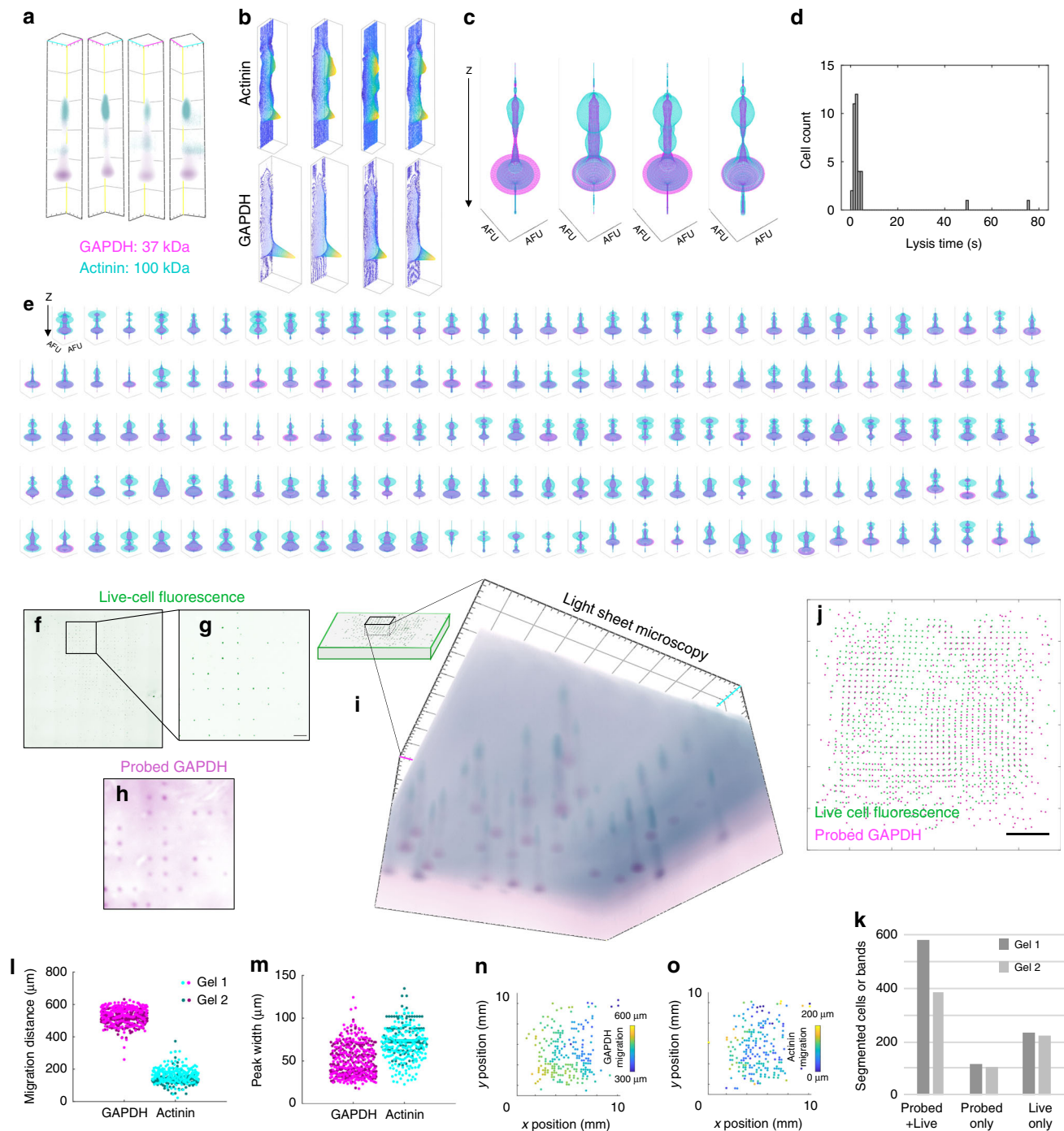
In formulating design guidelines for the dual-function lysis-electrophoresis buffer, we consider two additional points. First, detergents such as SDS and Triton X-100 form micelles of size on the order of nanometers^{60,61}. Consequently, we explored the corollary hypothesis that size-exclusion partitioning^{62,63} of solutes hinders delivery of lysis reagents from PAG matrices. As PAG density negatively correlates with the in-gel concentration of size-excluded species⁶², we explored whether lower density (6%T vs. 20%T) polyacrylamide lysis gels may facilitate improved protein solubilization. By moving to 6%T lysis gels, we observed higher apparent GAPDH mobility ($1.08 \pm 0.03 \times 10^{-4} \text{ cm}^2/\text{V s}$ using 6%T lysis gel, compared with $0.83 \pm 0.08 \times 10^{-4} \text{ cm}^2/\text{V s}$ using 20%T lysis gel, $n = 12\text{--}14$ separation lanes) and potential reduction in protein band dispersion (Supplementary Figure 3). Second, strong chaotropes like urea solubilize proteins by

disrupting hydrogen bonds as well as electrostatic and hydrophobic interactions to unfold hydrophobic protein regions⁶⁴. Urea-based lysis buffers can solubilize different subsets of the proteome, as compared to RIPA-like buffers⁶⁵. High concentrations of urea (e.g., 8 M) can break down detergent micelles and disturb detergent-protein complexes^{66,67}. Urea, as a small molecule, is less susceptible to size-exclusion partitioning from hydrogels. Just as in other protein separations, the ideal lysis buffer depends on the system and target of interest⁶⁴. Analysis of another endogenous target protein, GAPDH, using the 8 M urea lysis buffer that better-solubilized β -tubulin also yielded protein peaks with low dispersion (Fig. 4i).

Lastly, we verified the device design suggested by analysis of the well-characterized protein ladder now for the analysis of mammalian cells using the optimized cell preparation protocol (Fig. 4j). We anticipated that the cell preparation may increase lysate diffusion from that assessed using the idealized protein ladder system in Fig. 3, both because diffusion of protein targets in each single-cell lysate occurs during the time required for lysis and solubilization and because single-cell PAGE is run at higher temperature ($\sim 37^\circ\text{C}$ vs. $\sim 4^\circ\text{C}$) to improve protein solubilization. As discussed above, microwell spacing dictates the achievable cell throughput on one device. After 10 s EP, we measured $\sigma_{xy} = 32 \pm 13 \mu\text{m}$ for GAPDH (36 kDa) in the xy plane. At $\Delta_{\text{well}} = 192 \mu\text{m}$ ($6\sigma_{xy}$), we estimate that $<0.3\%$ of the fluorescence signal from the GAPDH in each cell lysate should bleed into the neighboring lane. Thus, $\Delta_{\text{well}} = 200 \mu\text{m}$ is also sufficient to limit cross-contamination between adjacent separation lanes for GAPDH under these assay conditions.

Immunoblotting of protein targets from hundreds of single mammalian cells. We applied projection electrophoresis to immunoblotting analyses of well-characterized endogenous proteins GAPDH and actinin across populations of individual human BT474 breast cancer cells. As depicted in Fig. 5, projection electrophoresis concurrently analyzes hundreds of single cells by parallelized separation after near-simultaneous lysis. To expedite full-gel volumetric fluorescence readout of protein immunoblots, we employed light-sheet microscopy in Fig. 5. Comparison measurements using scanning laser confocal microscopy are presented in Supplementary Figure 4. Data processing allows us to visualize immunoblot readouts as maximum intensity projection 3D renderings (Fig. 5a), 2D contour plots showing xz fluorescence peaks for each fluorescence color channel (corresponding to a target/antibody pair) (Fig. 5b), and revolved 1D z -directional fluorescence intensity plots (Fig. 5c).

Cells lyse nearly simultaneously (Fig. 5d). Across 4 replicate experiments, 31/36 monitored cells (86%) lysed within 5 s of placing the lysis gel on top of the microwell gel. Of the 5 remaining cells (all within the same replicate), 2 lysed during the 80 s monitoring period while 3 did not, potentially due to a bubble between the two gels. This near-simultaneous lysis, combined with parallelized electrophoretic separation over the full gel (>1000 separation lanes), facilitates concurrent analysis of hundreds of single cells. Figure 5e depicts revolved 1D intensity profiles for the 159 separation lanes within a single projection electrophoresis gel that passed $R^2 (>0.7)$ for Gaussian fit to 1D z -intensity profile) and SNR (>3) quality control in both protein channels (222 lanes passed these quality controls in the GAPDH channel; 204 lanes passed in the actinin channel). The intensity profiles show a GAPDH peak at a depth of $552 \pm 54 \mu\text{m}$ and an actinin peak at a depth of $165 \pm 42 \mu\text{m}$ (median \pm one standard deviation). The profiles also show another peak in the actinin channel near the depth of the GAPDH peak, potentially due to off-target antibody binding and/or spectral bleed-through



between the channels (optical filter sets) of the light-sheet microscope.

Projection electrophoresis is compatible with multi-modal imaging of the intact cells before separation, as well as the separated protein bands after the assay. Pre-separation live-cell imaging of intact BT474 cells (Fig. 5f, g) correlated well with detected probed bands. The in situ separations facilitated by projection electrophoresis allow comparison of live-cell fluorescence – prior to projection immunoblotting (via wide-field fluorescence microscopy in Fig. 5f, g) – and endpoint probed GAPDH signal (via wide-field fluorescence microscopy in Fig. 5h and light-sheet microscopy in Fig. 5i). The analysis revealed appreciable spatial correlation between live cell imaging prior to separation and wide-field fluorescence images of separated

GAPDH (Fig. 5j–k). Comparison shows 63–74% of detected live cells are correlated with GAPDH detection. In two duplicate separations, 76 and 63% of detected live cells corresponded to probed GAPDH bands, 24 and 37% of detected live cells did not correspond to a probed GAPDH band, and 17 and 22% of probed bands did not visibly correspond to a live cell. This correlation (and potentially cell settling efficiencies and analysis throughput) could potentially be further improved in future work by encapsulating settled cells in hydrogel to mitigate cell loss/movement during manual gel transfer and electrophoresis stack setup.

We observe the expected differential in electrophoretic mobility and nearly equivalent peak widths for the GAPDH (37 kDa) and actinin (100 kDa) targets for a total of 507 (GAPDH) and 303

Fig. 5 Projection electrophoresis permits the simultaneous analysis of hundreds of single cells by concurrent separation after simultaneous lysis.

(a) Maximum intensity projection 3D renderings of example separation lanes read out by tiled light-sheet microscopy. (b) xz (y -summed) contour plots of background-subtracted actinin and GAPDH protein signal within the lanes depicted in (a). (c) Revolved z -intensity profiles (arbitrary fluorescence units, AFU, vs. z) for the four separation lanes depicted in (a, b). Each plot depicts z -directional intensity profiles (summed fluorescence within each xy ROI vs. z) for GAPDH (magenta) and actinin (cyan), revolved around the z -axis to generate 3D rendering of fluorescence distribution. (d) Histogram quantification shows 86% of U251 cells lyse within 5 s of initiating lysis. (e) Quantified fluorescence intensity data for $n = 159$ separation lanes passing quality control for both the GAPDH and actinin channels. Each plot depicts revolved z -intensity profiles. (f) Full-gel wide-field fluorescence image of calcein-stained live BT474 breast tumor cells before analysis. (g) Subset of the live cells from (f), within a 1.75×1.75 mm light-sheet microscopy field of view (scale bar depicts $200 \mu\text{m}$). (h) Post-separation wide-field fluorescence image of probed GAPDH signal within the same field of view as (g). (f-h) are representative of $n > 3$ separation gels. (i) Maximum intensity projection 3D rendering (representative of duplicate separation gels) of a light-sheet microscopy image (same field of view as (g, h)), showing 3D separations of GAPDH and actinin from tens of separation lanes, each corresponding to signal from the settled cells in microwells depicted in (f, g). (j) Overlay image of segmented spots corresponding to live BT474 cells in microwells (green) and probed GAPDH bands after separation (magenta), for the same separation gel depicted in (f, i). (k) Quantification of correspondence between the segmented live cells and bands (via intensity thresholding) within the same separation lanes as (j). (l) Quantified migration distances from a total of $n = 507$ (GAPDH) and $n = 303$ (actinin) lanes passing quality control in two projection electrophoresis gels. (m) Quantified z -direction peak widths for the same bands analyzed in (l). (n-o) Map of the variation in GAPDH (n) and actinin (o) electromigration distances across the xy gel area. Source data are provided as a Source Data file.

(actinin) single-cell separations across duplicate separation gels (Fig. 5l, m). In considering variation in electromigration, the coefficients of variation in electromigration are for GAPDH $\sim 8.5\%$ and for actinin $\sim 27\%$. Qualitatively, we observe modestly higher electromigration on one side of the gel, on each of two gels (Fig. 5n, o, Supplementary Figure 5), which is inconsistent with Joule heating-induced electromigration nonuniformity (e.g., higher mobility in the gel center, as observed in bulk separations⁴²). Consequently, we attribute the modest, observed electromigration variation to nonuniformities in protein solubilization or electrophoresis (e.g., E and/or temperature), or to inaccuracies in gel surface detection ($z = 0$) during light-sheet image analysis. Including a protein-sizing ladder in each separation lane enhances size-based protein identification, as our group has reported in similar 2D single-cell immunoblot devices (either as a ladder of well-defined, cell-endogenous proteins³³ or as ladder protein-conjugated beads⁶⁸). Although from diffusion theory we would expect a larger peak width for the smaller protein target, differences in peak dispersion between targets can result in wider measured peak widths.

We compared scanning laser confocal microscopy (Supplementary Figure 4) and light-sheet microscopy (Fig. 5) imaging of the same gel devices to acquire volumetric protein immunoblot readouts from the protein PAGE separation lanes. Each imaging modality presents a trade-off in field of view and z -axis resolution, but the imaging throughput of light-sheet microscopy was $>10\times$ higher than scanning laser confocal, moving from ~ 120 s/lane readout time down to ~ 8 s/lane, while retaining sufficient z -axis resolution to localize protein peaks. The laser scanning confocal imaging with $20\times$ NA = 1.0 water immersion objective (required for high-resolution optical sectioning) supported a $425 \times 425 \mu\text{m}$ field of view, while light-sheet microscopy with $5\times$ detection objective (NA = 0.16) provided a much larger 1.75×1.75 mm field of view. Because its optical sectioning is facilitated by the light-sheet objectives forming a thin illumination sheet, light-sheet microscopy allows the imaging optical section thickness to be decoupled from the detection objective NA, facilitating the use of lower NA detection objectives while maintaining optical sectioning⁶⁹. The light-sheet images acquired here had optical section thicknesses on the order of $10 \mu\text{m}$, which should be sufficient to assess the diffusion-limited z -directional peak widths of tens of microns for our separated protein bands.

Further, light-sheet microscopy detected both protein targets with similar expected differential electrophoretic velocity and comparable peak widths of the immunoprobed targets to those measured with confocal (Supplementary Figure 4). Differences

may be partly attributed to the impact of a slight refractive index mismatch between the hydrogel and water immersion media on apparent confocal z -depths (Supplementary Note 1). With both readout modalities, we also observe the log-linear relationship between migration distance and molecular mass for endogenous targets that would be expected for a size-sieving separation (Supplementary Figure 6). Given similar results in detection, migration location, and peak width for the model endogenous protein targets, the substantially larger field of view of light-sheet microscopy proved beneficial, allowing endpoint imaging and analysis of $10\times$ larger number of immunoblots (imaged separation lanes passing quality control: $n = 22$ with confocal; $n = 303$ actinin and $n = 507$ GAPDH with light-sheet microscopy, over two separation gels).

The parallel cell analysis approach described here overcomes shortcomings of serial analysis of cells. Although synchronous cell lysis is also not instantaneous across cells (with biological variation in lysis time on the order of seconds⁷⁰), serial interrogation of individual cells leads to asynchronous analysis with longer time delays between analysis of the first cell and last cell in a population. Considering one published example single-cell enzyme analysis separation, where individual cells are interrogated by a capillary sampler after cell lysis via a UV light pulse¹⁷, we estimate a 104 min delay between interrogation of the first cell and interrogation of the last cell (219 cells analyzed with an analysis throughput of 2.1 cells/min). In contrast, concurrent analysis of ~ 300 measurable separation lanes is completed with <10 s delay between the first and last cell, assuming a small delay in cell lysis arising during the application of the lysis and solubilization buffer. Furthermore, projection electrophoresis uses a single SDS-PAGE sieving gel for hundreds of concurrent single-cell protein-sizing separations. In contrast, serial electrophoresis separations performed in capillaries or microchannels require periodic renewal of the sieving matrix between separations to mitigate residual sample and matrix degradation⁷¹. Consequently, higher-throughput electrophoresis systems often use free solution¹⁷ or sieving polymers²⁸. By introducing a new, rapid, and parallelized electrophoresis approach, we demonstrate simultaneous single-cell separations of hundreds of single cells with an active assay time of 2.5 cells/s (from lysis through photocapture), depending on settling efficiency — this represents a >70 -fold improvement in assay throughput over serial capillary systems.

Projection electrophoresis addresses key bottlenecks in single-cell protein analysis by achieving rapid (<1.5 min active assay time), synchronous size-based protein separation for hundreds of

unfixed cells in parallel, without sample transfer steps that can result in sample losses and changes in sample composition. Detection specificity combines antibody recognition with size-separation to confer proteoform-level specificity even when specific probes do not exist, and avoids the need for pre-separation tagging of proteins for detection. In situ cell lysis, separation, and photocapture of protein to the gel matrix mitigates deleterious effects of sample transfer between systems, including losses from adsorption to glassware, potential sample contamination, and sample changes between lysis and separation. Effectively synchronous analysis of hundreds of cells in parallel mitigates artifactual changes in cell population heterogeneity induced by heterogeneous lysis times, while also facilitating high assay throughput. Using rapid whole-cell lysis of unfixed cells, we demonstrate the detection of both nuclear and cytosolic proteins. We design and characterize the system by both modeling and measuring the results of microscale physics. Compared with planar (2D) single-cell western blotting, we demonstrate a 10-fold reduction in the volume of cell suspension settled (and thus the number of cells used) to assay the same number of cells, and further throughput improvements may be possible by optimizing parameters for settling efficiency. While 2D devices are conducive to immunoprobng, imaging as readout, and efficient data analysis, projection electrophoresis increases the density of single-cell analyses for the same device footprint, by shifting the separation dimension to the *z*-axis, while maintaining similar protein losses and outputting rich 3D information about protein band morphology and dispersion. Important beyond enhancing data density, 3D projection electrophoresis holds promise for future profiling of cellular “connectomes” by supporting analyses of complex cellular networks such as intact tissue slices and adherent cells cultured on planar hydrogel surfaces³⁷. Looking forward, the performance of projection electrophoresis can be improved in future work by moving to larger-area gels to further parallelize analysis, and by using our understanding of the driving small-scale physics to optimize gel materials for targets of interest and thus enable the use of even higher microwell densities (or adherent cells) and improved separation performance. With a straightforward, open microfluidic format and advantages complementary to existing protein analysis tools, we anticipate that projection electrophoresis will assist in the development of proteoform-level atlases of single-cell diversity.

Methods

Wafer microfabrication and silanization. Wafers with 40 μm -high features (32 μm diameter microwells for purified protein experiments and lysis monitoring, or 25 μm diameter microwells for BT474 and U251 single-cell separations) fabricated using SU-8 3050 (Microchem, now Kayaku Advanced Materials, Inc.) were fabricated according to the manufacturer’s instructions and then silane-treated⁷². Silicon wafers (WaferPro C04009) were cleaned by 5-minute agitated immersion in acetone followed by rinsing in acetone, isopropanol, and deionized water. Wafers were then dried under a nitrogen stream and dehydrated by a 10-minute bake on a hotplate set to 200 °C. Immediately after cooling, SU-8 3050 was spin-coated onto the wafers using a spin program consisting of 10 s at 500 RPM with an acceleration of 100 RPM/s followed by 30 s at 4000 RPM with an acceleration of 500 RPM/s. The resist was soft baked for 2 min on a 65 °C hotplate followed by 15 min on a 95 °C hotplate and finally 3 min on a 65 °C hotplate. The resist was exposed to UV light within a mask aligner for 10.8 s at an optical power of 29.26 mW/cm² (for an exposure dose of 316 mJ/cm²), through a transparency mask (CAD/Art Services, Inc.) and a longpass optical filter (Omega PL-360LP) (both of which attenuate the dose applied to the wafer below the 316 mJ/cm² stated above). After exposure, each wafer was post-exposure baked for 1 min at 65 °C, 5 min at 95 °C, and 1 min at 65 °C and cooled slowly by convection. Once cooled to room temperature, the features were developed in SU-8 developer (Microchem, now Kayaku Advanced Materials, Inc.) for 2.5–3 min on a shaker followed by 30–60 s spraying with fresh developer. The wafer was then rinsed by spraying with isopropanol to pool and cover both sides of the wafer 5 times, and then dried under a nitrogen stream. Finally, the resist was hard-baked for 30 min at 200 °C and then slowly ramped down to room temperature in 40 °C increments every 20 min. The patterned wafer was treated to facilitate gel release using vapor deposition of dichlorodimethylsilane

(Sigma-Aldrich 440272-100 ML) in a desiccator⁷³. Within a chemical fume hood, wafers were placed face-up in a desiccator and ~50–100 μL of liquid dichlorodimethylsilane was deposited into a 35 mm petri dish inside the desiccator. The desiccator was then immediately closed and connected to vacuum after a 1-minute waiting period. The desiccator was evacuated for 5 min; the vacuum was then switched off, desiccator valve closed, and silane left to settle under vacuum for 30 min. The desiccator valve was then slowly opened and wafers rinsed with deionized water and dried under a nitrogen stream.

Polyacrylamide gel fabrication. Substrate-free and featureless PAGs (used for lysis and enclosing purified protein microwells) were fabricated between a glass plate (McMaster-Carr) and 25 \times 75 mm or 50 \times 75 mm glass slide (VWR), both treated with Gel Slick® glass plate coating according to the manufacturer’s instructions and rinsed briefly in deionized water prior to gel fabrication. For purified protein experiments and cell-settling gels, microwell-stippled gels were cast between a methacrylate-functionalized glass slide and a silicon wafer patterned with microposts and silane-treated as described above. The methacrylate-functionalized slide was treated to promote gel adhesion with a 30-minute exposure to a degassed aqueous solution of 20% 3-(Trimethoxysilyl)propyl methacrylate (Sigma-Aldrich 440159-100 ML) and 30% acetic acid (Fisher A38212) in deionized water, and subsequently rinsed in pure methanol and deionized water and then dried under a nitrogen stream⁷².

Our approach for substrate-free micropatterned gel fabrication was inspired by that recently developed by our group to fabricate releasable gel microparticles⁷³. In all cases, 1 mm or 500 μm -thick gels were fabricated using spacers of the appropriate thickness (C.B.S Scientific Gel Wrap) between the two glass pieces or between the wafer and glass slide. Acrylamide precursor solutions for the various gels were prepared by diluting 30% stock acrylamide/bis-acrylamide precursor (Sigma-Aldrich A3699) and Rhinohide® (ThermoFisher R33400) solution (to increase mechanical robustness of substrate-free gels) in ultrapure water (Millipore®) and 10 \times tris-glycine (Bio-Rad 1610734) where appropriate. Separation gels contained 3 mM final concentration BPMA: N-(3-(3-benzoylphenyl)formamido)propyl methacrylamide, which was custom-synthesized by PharmAgra Labs (cat. no. PAL0603)⁷². BPMA is co-polymerized into the gel matrix and permits photo-immobilization of proteins. Gels were chemically polymerized for 60 min with 0.08% (w/v) ammonium persulfate (APS, Sigma-Aldrich A3678) and 0.08% (v/v) TEMED (Sigma-Aldrich T9281), from freshly-prepared 10% stock solutions in ultrapure water. The constituents of the various gel types used in this work are presented in Supplementary Table 1, and a schematic showing the released gel fabrication and molding process is depicted in Supplementary Figure 7.

After polymerization, gels were trimmed to size using a razor blade and released from the glass substrate by carefully sliding the razor blade under the gel, applying firm pressure with the blade onto the glass and gently adding water between the razor blade and gel to lubricate and prevent tearing. Separation and shield/lysis gels were stored in the appropriate buffer solution for a minimum of 12 h and up to 4 days prior to running separations. Buffer storage conditions are presented in Supplementary Table 1 and were either (1) dual function lysis-electrophoresis modified RIPA buffer (1 \times or 2 \times RIPA as described in Supplementary Table 2), (2) run buffer (1 \times tris-glycine with 0.5% Triton X-100), or (3) 1 \times tris-glycine for gels to be used for cell settling. Buffers used in this work are described in Supplementary Table 2.

Z-directional electrode system. The *z*-directional electrode separation system consists of planar electrodes integrated into a custom laser-fabricated acrylic alignment setup and brought into contact with two 32 mm diameter, 3 mm-thick neodymium rare-earth magnets on the backside of each electrode (each magnet specified to provide 19 lbs of pull force). Uniform spacing between the electrodes is facilitated by 2.5 mm (purified protein experiments) or 3 mm (cell experiments) removable polymer spacers (C.B.S Scientific Gel Wrap) at the top and bottom of the electrodes. The planar electrodes were commercial platinum-coated electro-transfer anodes (Bio-Rad Criterion anode plates) with plastic housings modified to permit close proximity of the electrode surfaces. Electric fields were provided by a power supply (Bio-Rad PowerPac® Basic) connected to the electrodes with standard banana plug interfacing. Cold packs on the back side of each electrode maintained gel temperature at ~4 °C to help to mitigate deleterious effects of Joule heating during purified protein separations. To aid in lysis and protein solubilization⁷⁴, the cold packs were heated in a 55 °C water bath for single-cell separations, yielding electrode temperatures of ~37 °C. Hot packs were heated for >10 min to equilibrate to temperature, and exchanged every ~15 min between separations.

Purified protein separation experiments. Mixed molecular mass purified protein solutions were prepared by diluting stock solutions of Alexa Fluor®555-labeled bovine serum albumin (BSA; Thermo Fisher Scientific A34786; 5 mg/mL stock), Alexa Fluor®488-labeled ovalbumin (OVA; Thermo Fisher Scientific O34781; 2 mg/mL stock), and Alexa Fluor®647-labeled donkey anti-mouse secondary antibody (IgG; Thermo Fisher Scientific A31571 lot 1900251; 2 mg/mL stock) in a run buffer (Supplementary Table 2) consisting of 1 \times tris-glycine (prepared by

ultrapure water dilution of 10× stock, Bio-Rad 1610734) containing 0.5% (v/v) Triton X-100 (Sigma). High molecular mass purified protein solutions were prepared by diluting stock solutions of Alexa Fluor®488-labeled lectin (Thermo Fisher Scientific L11270; 2 mg/mL stock), and Alexa Fluor®647-labeled transferrin (Thermo Fisher Scientific T23366; 5 mg/mL stock) in the same run buffer. All proteins were diluted to a final concentration of 5 μM.

Western blotting filter paper of 1 mm thickness (Thermo Fisher Scientific 84783) was cut into 12 × 12 mm squares and allowed to equilibrate in dual-function lysis-electrophoresis modified RIPA buffer for >10 min prior to starting separations. Microwell-patterned separation gels of 1 mm thickness and shield gels of 500 μm thickness were prepared as described in Supplementary Table 1, cut into squares of 9 × 9 mm (separation gel) or ~12 × 12 mm (shield gel) on a glass plate on top of a printed size guide, and equilibrated in the appropriate buffer for >12 h.

We first assessed the appropriate constant current conditions to yield the target electric field. We set up a dummy separation stack consisting of the anode (bottom), the buffer-equilibrated filter paper, a separation gel, a shield gel (with bottom surface dried by placing on a clean, dry Kimwipe™), and the cathode (top). We supplied a constant voltage of 13 V (the necessary voltage for an electric field of 52 V/cm) and noted the initial current through the dummy stack (typically ~33 mA). This constant current was chosen for each following separation run on a given day, and the initial and final voltages were noted during each trial to quantify the electric field and resistance changes during the separation.

To run the separations, we again stacked the anode, buffer-soaked filter paper, and separation gel, but this time dried the top (microwell-studded) surface of the separation gel gently bringing it into contact with a folded Kimwipe™ prior to stacking on top of the filter paper. Drying the top surface of the separation gel and bottom surface of the shield gel reduces dilution of the purified protein solution prior to separation. We pipetted 3 μL of the mixed purified protein solution (either the mixed molecular mass standard or the high molecular mass standard) on top of the separation gel and spread the resulting droplet to cover the surface of the gel using the side of a p20 pipette tip, taking care not to puncture the gel surface. We then dried the bottom side of a shield gel by placing it on a folded Kimwipe™, brought it into contact with the separation gel by carefully lowering it from one corner to reduce bubble entrapment, and assembled the cathode on top. We supplied constant current between the anode and cathode for varying electrophoresis times, running duplicate gels for each electrophoresis time in each experiment.

Immediately after electrophoresis was complete, the power was shut off and the system disassembled to permit optical access for a UV source (Hamamatsu Lightningcure LC5). The liquid light guide-coupled UV source was used to photocapture the separated protein bands using a 45 s UV exposure, holding the tip of the liquid light guide ~4 cm from the separation gel. We have photocaptured with both the top (microwell) and bottom (flat) side of the separation gel facing the light guide. The total time between beginning electrophoresis and initiating UV exposure was recorded for each test as an estimate of the in-gel diffusion time t_{diff} .

After photocapture, each gel was rinsed briefly in deionized water and then stored for >12 h in 1× tris-buffered saline solution with Tween® (TBST, prepared from Cell Signaling Technology 9997 S 10× stock and MilliQ ultrapure water) in a polystyrene 12-well plate prior to imaging to permit release of any non-photocaptured protein. Gels were imaged through a #1 coverslip using a Zeiss LSM 880 laser-scanning confocal microscope fitted with a 20× water dipping objective (NA = 1.0, Zeiss W Plan APO 20x/1 DICIII). A confocal z-slice spacing of 5 μm was chosen, and volumes extending ~100 μm past visible fluorophore bands were imaged. As we were not quantifying or comparing protein abundance, excitation laser powers were adjusted to permit fluorescence visibility depending on the sample brightness. Fluorescence intensities were not compared between purified protein samples. Similarly, images were brightness and contrast-adjusted in Fiji⁷⁵ (based on ImageJ⁷⁶, National Institutes of Health) to ensure visibility of protein bands. Maximum intensity projection 3D renderings were prepared in Zeiss Zen Blue software.

Purified protein confocal datasets were analyzed using custom analysis scripts in MATLAB®. The scripts were designed to (1) find and track regions of interest (ROIs) corresponding to protein originating from each of the microwells through the depth of each confocal stack, (2) create 1D intensity plots of summed fluorescence intensity vs. z depth for each ROI by summing the fluorescence intensity for the ROI at each z-plane, (3) assess the z migration distance and peak width for each protein by Gaussian fitting each intensity profile peak, allowing the user to set bounds for fitting peaks corresponding to each purified protein, (4) measure the diffusional spreading of protein from each microwell by Gaussian fitting the summed 1D x- and y-intensity profiles for each protein at its z migration peak location for each protein, (5) plot migration distance, z-direction peak width, and xy peak width vs. electrophoresis time or diffusion time, comparing across multiple gels.

Zeiss CZI confocal z-stacks and associated metadata were imported into MATLAB® (MathWorks®) using the MATLAB® Bio-Formats libraries provided by the Open Microscopy Environment⁷⁷. ROIs were segmented in each z-slice image (summing the intensities of all color channels into one image for the purposes of segmentation) using intensity thresholding followed by morphologic open and close operations to remove erroneously-segmented small features and close incomplete contours. A fill operation was then used to close all holes in the segmented spots of protein, and all segmented objects touching the border of the

image were removed. The centroids of the segmented spots of protein at each z location were stored, and a MATLAB® particle tracking library (based on a previous IDL implementation⁷⁸) made publicly accessible by Prof. Daniel Blair and Prof. Eric Defresne⁷⁹ was used to track the positions of protein originating from each microwell through the z depth of the image. The tracked centroids were then subject to a quality control step to remove protein spots that were only found in small portions of the full z volume. After this was complete, the tracking code output a set of tracked ‘particles’ (protein spots originating from a given microwell), each with a list containing the xy location of the centroid of each protein spot for every z location in the image. To create the intensity profiles, the intensities in a 300 pixel (102 μm) square ROI were analyzed surrounding each centroid at each z location. The data were background-subtracted by subtracting from each pixel the average measured intensity 15 μm below the bottom of the microwells, in regions at least 100 pixels (34 μm) from any segmented protein spots. After Gaussian fits to find the migration distance, z-direction peak width, and xy peak width for each protein peak, the data from all of the ROIs from multiple gels (multiple electrophoresis times in duplicate) were plotted and fit to the expected linear physical relationship (migration distance vs. electrophoresis time, squared peak width and squared xy peak width vs. total in-gel time).

Cell culture. U251 human glioblastoma cells stably transduced with TurboGFP by lentiviral infection were kindly provided by Prof. Sanjay Kumar’s laboratory at UC Berkeley (the naive, pre-modification U251 cell line was obtained from the UC Berkeley Tissue Culture Facility, originally sourced from the American Type Culture Collection). Cells were maintained in tissue culture flasks in a standard cell culture incubator (Heracell 150i) at 5% CO₂ and 37 °C, in DMEM (Invitrogen 10566016) supplemented with 10% FBS (Gemini Bio-Products Benchmark 100–106), 1% penicillin/streptomycin (Life Technologies 15140-122), 1× sodium pyruvate (Thermo Fisher 11360070), and 1× non-essential amino acids (Life Technologies 11140-050 100× stock). The cells were passaged at a density of 1:10 to 1:40 after reaching ~80% confluency by detaching with 0.05% Trypsin-EDTA (Life Technologies 25300120), centrifuging for 3 min at 1000 RPM, and resuspending in complete media to reseed.

BT474 human breast cancer cells were purchased from the UC Berkeley Biosciences Divisional Services Cell Culture Facility. Cells were maintained in tissue culture flasks in a standard cell culture incubator (Heracell 150i) at 5% CO₂ and 37 °C, in DMEM (Invitrogen 10566016) supplemented with 10% FBS (Gemini Bio-Products Benchmark 100–106) and 1% penicillin/streptomycin (Life Technologies 15140-122). The cells were passaged at a density of 1:2 to 1:8 after reaching ~80% confluency by detaching with 5 mM EDTA in PBS (Invitrogen 15575-038 diluted in sterile 1× PBS: Life Technologies 10010049), centrifuging for 3 min at 1000 RPM, and resuspending in complete media to reseed.

Cell lysis monitoring experiments. We compared diffusion profiles of cells lysed after settling in 32 μm diameter, 40 μm high microwells within 1 mm-thick gels. Microwell gels and lysis gels (18 × 18 mm in area) were prepared and equilibrated in PBS for >12 h, as described above.

To settle cells in microwells, we followed a procedure similar to that used for single-cell western blotting⁷². U251-TurboGFP cells were detached using 0.05% trypsin-EDTA (Life Technologies 25300120), resuspended in PBS (Life Technologies 10010049) at a concentration of 100 000 cells/mL, and filtered using a cell strainer (Corning 352235). The 18 × 18 mm microwell gels were placed microwell side up in a 60 mm tissue culture dish. ~100 μL cell solution was pipetted onto the surface of each microwell gel (to cover but avoid spillage over the edge of the gel) and spread to cover the full array of microwells. The cells were allowed to settle for 5 min on ice, gently agitating every ~2 min, before rinsing with 1–3 mL PBS by tilting the tissue culture dish at a ~40° angle, pipetting PBS at the top surface of the microwell gel, and allowing it to flow over the surface of the microwell gel into the bottom of the petri dish. After rinsing was complete, the excess PBS/cell solution was aspirated for biohazard disposal.

To facilitate monitoring, each microwell gel was immobilized within a 60 mm petri dish by pipetting 200 μL of a warmed solution of 5% agarose (Invitrogen 16500) in PBS (Life Technologies 10010049) beside the gel and allowing it to gel at room temperature (in contact with the edge of the gel and the petri dish). Before lysis, excess fluid was removed from the gel by tilting the petri dish and wicking away the fluid layer by bringing a folded Kimwipe™ into contact with the corner of the gel (not touching cell-containing regions). The petri dish was then secured to the stage of an Olympus IX71 microscope for monitoring with a 4× or 10× air objective. Fluorescence excitation was provided by an X-Cite source (Excelitas Technologies) through a GFP filter set (Chroma 49011 ET), and fluorescence was measured using an EM-CCD camera (Andor iXon). Time-lapse images of the TurboGFP fluorescence were captured using the MetaMorph® imaging software (Molecular Devices). After focusing, setting up the imaging settings and initiating the time-lapse, the lysis gel was carefully placed on top of the cell-containing gel, starting with one corner and then smoothly bringing the rest in contact to reduce bubble entrapment between the two gels. The time at which the lysis gel was placed in the time-lapse series was recorded. The lysis gel was a 20%T, 10% Rhinohide® shield gel equilibrated in 2× RIPA-like lysis buffer.

The lysis monitoring data were analyzed using custom scripts written in MATLAB®. At each time point, the cells were segmented using adaptive

Table 1 Protein hydrodynamic radii (r_H), diffusion coefficients (D) and partition coefficients (k) used in finite-element modeling of diffusion during lysis and electrophoresis.

Protein	r_H [nm]	D_{sol} [m^2/s]	$D_{7\%T}$ [m^2/s]	$D_{20\%T}$ [m^2/s]	$k_{7\%T}$	$k_{20\%T}$
TurboGFP	2.3	6.61×10^{-11}	1.36×10^{-11}	9.49×10^{-13}	0.501	0.0415
BSA	3.01	5.05×10^{-11}	7.90×10^{-12}	3.49×10^{-13}	0.344	0.00744
HER2	3.76	4.04×10^{-11}	4.88×10^{-12}	1.39×10^{-13}	0.213	8.16×10^{-4}

thresholding of the median-filtered (3×3 neighborhood) image. The segmentation was improved using morphologic open and close operations, and the centroids of the segmented cells were computed and stored. The MATLAB® particle tracking library (based on a previous IDL implementation⁷⁸) made publicly accessible by Prof. Daniel Blair and Prof. Eric Defresne⁷⁹ was used to track the centroids of each cell over the course of the experiment, although minimal drift was observed. The maximum fluorescence intensity and total fluorescence intensity in a 100 μ m diameter circle surrounding the centroid of each segmented cell were tracked for each time point. All pixel intensities were background-subtracted using the average fluorescence intensity of the background region at each time point, taken to be the image regions greater than 30 μ m away from all segmented regions.

Finite-element modelling of protein diffusion. We used finite-element modelling of dilute species transport in COMSOL® Multiphysics to predict protein concentrations during lysis and electrophoresis. The simulation geometries for the projection electrophoresis simulations are presented in the cross-sectional view shown in Fig. 4b. 2D axisymmetric models were used for all simulations due to the inherent symmetry of the geometry. Diffusion coefficients in free solution portions of the model were estimated from the Stokes-Einstein equation⁵⁰, while in-gel diffusion was estimated from the free-solution diffusivity using the methods presented by Park, et al.⁵¹. Protein hydrodynamic radii were estimated from the number of amino acids⁸⁰. Thermodynamic partitioning of protein was simulated using flux boundary conditions relating in-gel concentration to in-solution concentration using a partition coefficient $k = C_{gel}/C_{solution}$. Partition coefficients were estimated using the Ogsten model⁸¹ (assuming size-exclusion partitioning), using estimates of fiber radius from Tong and Anderson⁶² and hydrogel volume fraction from the data presented by Baselga, et al.⁸². A temperature of 4 °C was assumed for all simulations except the comparison with the single-cell western blot platform, which assumed 10 °C for both platforms. The diffusion and partition coefficients for each protein at 4 °C are presented in Table 1.

In each model, gel-solution boundaries were modeled as flux boundary conditions taking size-exclusion partitioning into account. The edges of each model were modeled as flux boundary conditions permitting protein to freely leave the model; however, the simulation region was sufficiently large (500 \times 500 μ m) that changing these boundary conditions to no flux resulted in negligible change to the modeled concentration profiles. The initial protein concentration in the cell region was 2 μ M, while the initial concentration elsewhere in the model was zero. In models of the single-cell western blotting platform, the bottom surface of the gel was modeled as no flux to model the presence of the glass slide present in that system. The model was meshed with a physics-controlled mesh calibrated for fluid dynamics, and a user-controlled override with maximum element size of 0.5 μ m was used in the microwell and thin fluid layer regions to ensure sufficient mesh density in these smaller regions.

A time-dependent study was used to model the protein concentration profile during lysis and electrophoresis. To model both in the same diffusive model, the diffusion and partition coefficients were set as step functions. For the first 25 s of the model (the lysis portion), the diffusion and partition coefficients were set as in Table 1. After this 25 s lysis period, all partition coefficients were set to 1, and the diffusion coefficients in all regions of the model were set to those for 7%T gel (the separation gel), effectively simulating instantaneous injection of the full protein profile into a separation gel. While this method is straightforward and does not require modelling of the electrophoresis physics, it provides a conservative (over-) estimate of z-directional diffusional spreading because it does not model stacking of the protein band as it is injected from free solution into the gel.

After running the model, we assessed the maximum protein concentrations in the simulated geometry. We also assessed the integrated protein intensities (the protein concentrations at each radial (x) location, integrated in z) to model the wide-field microscopy imaging measurements in which fluorescence from the full z region is integrated into a 2D image. These intensities were compared with the experimental lysis monitoring data.

Single-cell separations. Adherent U251 glioblastoma and BT474 breast tumor cells were detached from culture flasks with 0.05% Trypsin-EDTA (Life Technologies 25300120) (U251) or 5 mM EDTA (Invitrogen 15575-038) in PBS (BT474) and resuspended in cold PBS (Life Technologies 10010049) at a concentration of 1.5×10^6 cells/mL. For viability staining to aid in microwell occupancy assessment, BT474 cells were stained with Calcein-AM in incomplete DMEM for 20 min at room temperature prior to resuspension. Cell suspensions were kept on ice and

filtered through a cell strainer (Corning 352235) to reduce cell aggregates immediately prior to settling.

1 mm-thick micropatterned separation gels were stored in 1 \times tris-glycine (Bio-Rad) and buffer-exchanged to lower-conductivity sucrose-dextrose dielectrophoresis buffer (DEP buffer: 2.39 g/L HEPES (VWR 3638C017), 80.7 g/L sucrose (Sigma-Aldrich S0389), 4.5 g/L dextrose (Fisher D16-500), 11.1 mg/L CaCl₂ (FisherC79-500); pH adjusted to pH 7.5 with NaOH)⁸³ at least 10 min prior to cell settling. To settle the cells, gels were placed microwell side up inside of a 35 mm tissue culture dish. 25 μ L of single-cell suspension was supplied to each 9 \times 9 mm gel (by first pipetting 15 μ L onto the gel surface, spreading with a pipette tip while taking care not to perforate the gel surface, and subsequently dispensing another 10 μ L onto the surface. Cells were allowed to gravitationally settle for 20 min, agitating the gel periodically and covering the gel with the lid of the 35 mm tissue culture dish (to reduce evaporation). Settled cells were checked at the 10-minute mark, and if the cell suspension had aggregated towards the center of the gel, an additional 10 μ L of cell suspension was supplied to the gel edges.

After 20 min of settling, gels were rinsed by holding the petri dish at a ~40° angle and pipetting 0.5 mL of DEP buffer onto the top corner of the gel, allowing the fluid stream to wash over the full gel into the tissue culture dish. The wash fluid was aspirated for biohazardous waste disposal, and the wash was repeated with an additional 0.5 mL of DEP buffer before pipetting ~40 μ L DEP buffer on top of the gel to prevent drying during imaging. Tiled and stitched images of the settled cell fluorescence were captured using the ScanSlide plugin for the MetaMorph® imaging software (Molecular Devices), using an Olympus IX51 inverted wide-field fluorescence microscope fitted with an X-Cite® illumination source (Excelitas Technologies), GFP filter set (Chroma 49011 ET), 4 \times objective, and CoolSNAP HQ2 CCD camera (Teledyne Photometrics). Cell occupancy was calculated from a MATLAB® script that analyzed tiled live-cell brightfield and fluorescence images, determined whether there was a fluorescent object in a region surrounding each microwell (via thresholding segmentation) and, if found, displayed the region and prompted user input of number of cells in the microwell region.

Aliquots of lysis buffer (4 mL) were prepared by dissolving urea to a final concentration of 8 M in 2 \times RIPA-like lysis buffer in a water bath set to 55 °C. Lysis gels (14 \times 14 \times 1 mm) were stored in 2 \times RIPA-like lysis buffer and transferred to aliquots of urea lysis buffer as soon as the urea had dissolved (10–60 min prior to running the separations). The lysis gels in buffer aliquots were heated to 55 °C in a water bath until immediately prior to use, agitating periodically to ensure the solution was well mixed.

After cell settling and live-cell imaging, 4 mL 2 \times tris-glycine (diluted from Bio-Rad 1610734 10 \times stock) was pipetted into the tissue culture dish containing the separation gel and incubated for 1 min to reduce the concentrations of potentially unwanted ions. A 10 \times 10 \times 1 mm filter paper (cut to size from Thermo Fisher Scientific western blotting filter paper) was hydrated in the heated lysis buffer aliquot and placed on the anode. The separation gel was placed (microwell side up) on top of the filter paper immediately after tris-glycine incubation, placing slowly from one corner to reduce bubble entrapment between the layers. The lysis gel was removed from the buffer aliquot and placed on top of the separation gel, again placing gradually so as to not introduce bubbles between the gels. The lysis timer was started as soon as the lysis gel was placed, and the electrode system was closed by placing the cathode on top of the lysis gel. After 25 s lysis, the separation was initiated by supplying 80 mA of constant current (typically yielding 13–16 V initial voltage for an average electric field of 43–53 V/cm across the gel stack) using a DC power supply (Bio-Rad PowerPac Basic) and recording the voltage at 5 s intervals during electrophoresis. After electrophoresis was complete, the power supply was stopped, electrode system opened, and 45 s photocapture was completed using a Hamamatsu Lightningcure LC5 UV source. The gel was then rinsed briefly in deionized water before equilibrating in tris-buffered saline with Tween® (1 \times TBST, from Cell Signaling Technology 9997 S 10 \times stock) overnight to remove any residual lysis buffer (exchanging the buffer after 2 h). Projection electrophoresis gels probed with F(ab) fragments were blocked overnight in 5% BSA in TBST at 4 °C or for between 2–4 h on a shaker at room temperature prior to immunoprobng.

Immunoprobng and imaging. Single-cell projection electrophoresis immunoblotting gels were probed either diffusively (for initial characterization experiments using labeled F(ab) fragments in Fig. 4) or electrophoretically (using standard primary and fluorescently-labeled secondary antibodies in Figs. 1 and 5). All probing wash steps were performed using an electrophoretic wash platform.

In-gel probing requires high concentrations of immunoprobes to mitigate size-exclusion partitioning effects^{62,72}. To minimize reagent consumption, we probe

Table 2 Probe delivery gel fabrication parameters for electrophoretic and diffusive probing.

Gel type	Final agarose concentration after probe dilution	Antibody probes	Gelation time	Fabrication setup
Primary antibody electrophoretic probe delivery agarose gel	1.5% (w/v) (dissolved in 1× tris-glycine) UltraPure LMP Agarose, (Thermo-Fisher: 16520050)	For the studies reported in Fig. 5 and Supplementary Figures 4–6, dilutions from each stock were: (1) Rb α-actinin (1:15, 6.67% (v/v)) & (2) Gt α-GAPDH (1:10, 10% (v/v)). For the studies reported in Fig. 1 and Supplementary Figure 8, dilutions from each stock were: (1) Ms α-PTBP1 (1:10, 10% (v/v)) & (2) Gt α-GAPDH (1:10, 10% (v/v))	5 mins on ice pack	Glass plate and glass slide
Secondary antibody electrophoretic probe delivery agarose gel	1.5% (w/v) (dissolved in 1× tris-glycine) UltraPure LMP Agarose, (Thermo-Fisher: 16520050)	For the studies reported in Fig. 5 and Supplementary Figures 4–6, dilutions from each stock were: (1) Dk α-Rb AF555 (1:10, 10% (v/v)) & (2) Dk α-Gt AF488 (1:10, 10% (v/v)). For the studies reported in Fig. 1 and Supplementary Figure 8, dilutions from each stock were: (1) Dk α-Ms AF555 (1:20, 5% (v/v)) & (2) Dk α-Gt AF488 (1:20, 5% (v/v))	5 mins on ice pack	Glass plate and glass slide
hFAB diffusive probe delivery agarose gel	1.5% (w/v) - dissolved in 1× tris-buffered saline solution with Tween® (1× TBST, from Cell Signaling Technology 9997 S 10× stock) UltraPure LMP Agarose, (Thermo-Fisher: 16520050)	1:10 (10% (v/v)) dilution from stock of either: (1) Bio-Rad hFAB Rhodamine α-GAPDH or (2) hFAB Rhodamine α-tubulin	5 mins on ice pack	Glass plate and glass slide

single-cell western blotting gels using minimal solution volumes. For the projection electrophoresis system, larger probe volumes are required to probe thicker gels; as such, we deliver probes using thin (0.5–1 mm-thick) hydrogel layers to provide even probe delivery to all regions of the gel. Fluid, in contrast, tends to pool around gel edges, resulting in brighter probed signal at the gel edge. Constituents and fabrication parameters of probe delivery gels are described in Table 2.

For diffusive probe delivery, Bio-Rad hFAB probes for GAPDH (12004167) or tubulin (12004165) were mixed at a 1:10 dilution with low melting temperature agarose (Invitrogen 16520-050) solution. Agarose was dissolved in 1× tris-buffered saline solution with Tween® (TBST) to yield a final concentration of 1.5% (w/v) after probe dilution, and maintained on a hotplate with spin bar at a temperature of ~40 °C until mixing with the probes. The temperature of the solution immediately after mixing typically read ~30 °C. The agarose gel was then immediately cast from the agarose-probe solution by pipetting between a heated (to ~30 °C) glass plate and microscope glass slide, separated by gel casting spacers (C.B.S. Scientific GelWrap, 0.5 mm thickness). After casting, the glass plate setup was carefully moved onto a cold pack and the agarose was permitted to gel for 5 min before carefully disassembling the stack, cutting the gels to match the size of the separation gels, and immediately setting up the probing stacks. Each high-density separation gel was sandwiched between two 0.5 mm-thick agarose probe delivery gels in a dry well of a 24-well plate (with surrounding wells filled with water), sealed with a plate sealer, and incubated at 4 °C in the dark for 40 h.

For electrophoretic probe delivery, agarose probe delivery gels were fabricated in the same manner as the diffusive probe delivery gels described above; however, gels were fabricated at 1 mm thickness. Primary antibodies were electrophoretically introduced, incubated, and electrophoretically washed; this process was then repeated for fluorescently-labeled secondary antibodies. Primary antibodies used were Rb α-actinin (CST 6487, lot 2), Ms α-PTBP1 (Sigma WH0005725M1, lot J4241-3H8), and Gt α-GAPDH (Sigma SAB2500450, lot 6377C3); secondary antibodies were Dk α-Rb AF555 (Invitrogen A-31572, lot 2017396), Dk α-Ms AF555 (Invitrogen A-31570, lot 2045336), and Dk α-Gt AF488 (Invitrogen A-11055, lot 2059218). Immediately after casting the antibody probe delivery gel, a stack was set up for electrophoretic probe introduction. The probe delivery gel was placed against the flat (non-microwell-stippled) side of the separation gel, taking care not to introduce bubbles between the two buffer-soaked gels. The stacked gel setup was sandwiched between two pieces of buffer-soaked (1× tris-glycine with 0.5% Triton X-100) western blotting filter paper (Thermo Fisher Scientific 84783) held together using a laser-cut acrylic holder with a cut-out for the gel stacks. The holder was used to suspend the gels (with the separation gel facing the anode (+) and delivery gel facing the cathode (-)) in a slab-gel blotting module (Invitrogen X-Cell II) filled with 1× tris-glycine with 0.5% Triton X-100. Probes were transferred from the delivery gel into the separation gel using an electric field of 8 V/cm for 13 min; the stack was then disassembled and the separation gels were incubated at room temperature on a glass slide within a hydration chamber for 2 h for primary antibody binding, or 1 h for secondary antibody binding.

After each probe incubation step (primary and secondary antibodies), projection electrophoresis gels were electrophoretically washed by sandwiching between two filter papers soaked in 1× tris-glycine with 0.5% Triton X-100 (held in place by the same custom laser-cut acrylic with a cut-out for the gels, which suspended the gels within the chamber of a slab-gel blotting module). Separation gels were submerged in 1× tris-glycine with 0.5% Triton X-100 for ~1 min for rehydration immediately before electrophoretic washing. The blotting module was again filled with 1× tris-glycine with 0.5% Triton X-100. Gels were electrophoretically washed for 15 min using an electric field of 12 V/cm. Further details regarding the electrophoretic probing assay and its characterization, including comparison to diffusive probing, have been published by Mourdoukoutas, Grist, and Herr⁸⁴.

Gels were confocal imaged through a #1.5 coverslip using a Zeiss LSM 880 laser-scanning confocal microscope fitted with a 20× water dipping objective (NA=1.0, Zeiss W Plan APO 20x/1 DICIII). A confocal z-slice spacing of 5 μm was chosen, and volumes extending ~100 μm past visible fluorophore bands were imaged. As we were not quantifying or comparing protein abundance, excitation laser powers were adjusted to permit fluorescence visibility depending on the sample brightness, as fluorescence intensities were not compared between cell separations. Similarly, images were brightness and contrast-adjusted in Fiji⁷⁵ (based on ImageJ⁷⁶, National Institutes of Health) to ensure visibility of protein bands.

For full-gel imaging, gels were imaged using a Zeiss Lightsheet Z.1 system fitted with a 5× detection objective (Zeiss EC Plan-Neofluar 420330-8210) and 4× light-sheet objectives (Zeiss LSM 400900-9010). Samples were excited with 488 nm and 561 nm lasers and detected using two pco.edge sCMOS cameras (with filter sets for AlexaFluor® 488 and AlexaFluor® 555). The samples were mounted to #1.5 coverslips using superglue at the gel corners, and the coverslip was glued to a custom 3D printed adapter to suspend the gel within the imaging chamber. The gels were imaged facing the detection objective (not imaged through the mounting coverslip). Tiled z-stack images with 5–6 μm z-slice spacing were acquired over the full gel volume, with 10% overlap between acquisition fields of view to ensure complete gel coverage. 49–56 z-stack fields of view were typically required to cover the full gel area, each with 200–300 z-slices.

Confocal and light-sheet microscopy datasets were analyzed using custom analysis scripts in MATLAB®, similar to those described above for purified protein datasets. Zeiss CZI confocal z-stacks and associated metadata were imported into MATLAB® (MathWorks®) using the MATLAB® Bio-Formats libraries provided by the Open Microscopy Environment⁷⁷. The analysis workflow is described in Supplementary Figure 8. 3D datasets are made up of 2D (xy) slice images that are each processed to assess the 3D positional data for each separated protein peak. Intensity profiles were background-subtracted by subtracting the average intensity of a 5-pixel (light-sheet) or 20-pixel (confocal) border surrounding each xy ROI from each ROI pixel at each z location prior to summing the intensities to generate z-intensity profiles. Thin (10-pixel for confocal and 5-pixel for light-sheet) borders

between the ROI and background regions were used to assess the background-subtracted noise of the measurement to compute signal-to-noise ratios for each protein peak. Protein peaks corresponding to separation lanes were quantified (passing quality control) if: (1) there was a segmented fluorescence spot, (2) the Gaussian fit to the *z*-intensity profile of the peak region had an R^2 of the Gaussian intensity profile fit of >0.7 , and (3) the Gaussian fit had a signal-to-noise ratio (Gaussian peak fit amplitude divided by twice the standard deviation of the background-subtracted noise calculation region over the *z* region of the protein peak) of >3 . A schematic representing the analysis workflow for tiled light-sheet images (similar to the workflow used for confocal images but with the addition of functionality to find and analyze separation lane ROI locations across multiple image tiles/“series”) is presented in Supplementary Figure 9.

Reporting summary. Further information on research design is available in the Nature Research Reporting Summary linked to this article.

Data availability

The datasets generated and analyzed as a part of this work are available in the Dryad repository in the main data publication (<https://doi.org/10.6078/D1B13V>) and linked data publications (<https://doi.org/10.6078/D1N989>, <https://doi.org/10.6078/D1811G>, <https://doi.org/10.6078/D1HH6C>). Source data for Fig. 1(g), 2(c–e), 3(d–h), 4(e–g), 5(d, e, j–o) and Supplementary Figs 1, 4, and 6 are also provided as a Source Data file. Source data are provided with this paper.

Code availability

All custom analysis code generated as a part of this work is available from the corresponding author upon reasonable request. Custom MATLAB scripts central to this work are deposited in a GitHub repository: https://github.com/samanthagrist/projection_cp_analysis.

Received: 28 February 2020; Accepted: 20 October 2020;

Published online: 04 December 2020

References

- Berg, J. M., Tymoczko, J. L. & Stryer, L. *Biochemistry. 5th edition. Chapter 3: Protein Structure and Function.* <https://www.ncbi.nlm.nih.gov/books/NBK21177/> (W. H. Freeman, 2002).
- Vogel, C. et al. Sequence signatures and mRNA concentration can explain two-thirds of protein abundance variation in a human cell line. *Mol. Syst. Biol.* **6**, 1–9 (2010).
- Darmanis, S. et al. Simultaneous multiplexed measurement of RNA and proteins in single cells. *Cell Rep.* **14**, 380–389 (2016).
- Liu, Y., Beyer, A. & Aebersold, R. On the dependency of cellular protein levels on mRNA abundance. *Cell* **165**, 535–550 (2016).
- Gong, H. et al. Single-cell protein-mRNA correlation analysis enabled by multiplexed dual-analyte co-detection. *Sci. Rep.* **7**, 1–8 (2017).
- Smith, L. M. & Kelleher, N. L. Consortium for Top Down Proteomics Proteoform: a single term describing protein complexity. *Nat. Methods* **10**, 186–187 (2013).
- Harper, S. J. & Bates, D. O. VEGF-A splicing: the key to anti-angiogenic therapeutics? *Nat. Rev. Cancer* **8**, 880–887 (2008).
- Arribas, J., Baselga, J., Pedersen, K. & Parra-Palau, J. L. p95HER2 and breast cancer. *Cancer Res.* **71**, 1515–1519 (2011).
- Liu, Y., Chen, X., Zhang, Y. & Liu, J. Advancing single-cell proteomics and metabolomics with microfluidic technologies. *Analyst* **144**, 846–858 (2019).
- Kennedy, R. T., Oates, M. D., Cooper, B. R., Nickerson, B. & Jorgenson, J. W. Microcolumn separations and the analysis of single cells. *Science* **246**, 57–63 (1989).
- Naing, L., Winn, T. & Rusli, B. N. Practical issues in calculating the sample size for prevalence studies. *Arch. Orolfac. Sci.* **1**, 9–14 (2006).
- Spruessel, A. et al. Tissue ischemia time affects gene and protein expression patterns within minutes following surgical tumor excision. *Biotechniques* **36**, 1030–1037 (2004).
- Lee, T. T. & Yeung, E. S. Quantitative determination of native proteins in individual human erythrocytes by capillary zone electrophoresis with laser-induced fluorescence detection. *Anal. Chem.* **64**, 3045–3051 (1992).
- Olefirowicz, T. M. & Ewing, A. G. Dopamine concentration in the cytoplasmic compartment of single neurons determined by capillary electrophoresis. *J. Neurosci. Methods* **34**, 11–15 (1990).
- Simpson, P. C. et al. High-throughput genetic analysis using microfabricated 96-sample capillary array electrophoresis microplates. *Proc. Natl Acad. Sci. USA* **95**, 2256–2261 (1998).
- Rogers, B., Gibson, G. T. T. & Oleschuk, R. D. Bundled capillary electrophoresis using microstructured fibres. *Electrophoresis* **32**, 223–229 (2011).
- Dickinson, A. J., Armistead, P. M. & Allbritton, N. L. Automated capillary electrophoresis system for fast single-cell analysis. *Anal. Chem.* **85**, 4797–4804 (2013).
- Hargis, A. D., Alarie, J. P. & Ramsey, J. M. Characterization of cell lysis events on a microfluidic device for high-throughput single cell analysis. *Electrophoresis* **32**, 3172–3179 (2011).
- Wheeler, A. R. et al. Microfluidic device for single-cell analysis. *Anal. Chem.* **75**, 3581–3586 (2003).
- Bandura, D. R. et al. Mass Cytometry: Technique for Real Time Single Cell Multitarget Immunoassay Based on Inductively Coupled Plasma Time-of-Flight Mass Spectrometry. *Anal. Chem.* **81**, 6813–6822 (2009).
- Budnik, B., Levy, E., Harmange, G. & Slavov, N. SCOPE-MS: mass spectrometry of single mammalian cells quantifies proteome heterogeneity during cell differentiation. *Genome Biol.* **19**, 161 (2018).
- Zhu, Y. et al. Proteomic analysis of single mammalian cells enabled by microfluidic nanodroplet sample preparation and ultrasensitive nanoLC-MS. *Angew. Chem. Int. Ed. Engl.* **57**, 12370–12374 (2018).
- van Remoortere, A. et al. MALDI imaging and profiling MS of higher mass proteins from tissue. *J. Am. Soc. Mass Spectrom.* **21**, 1922–1929 (2010).
- Aichler, M. & Walch, A. MALDI Imaging mass spectrometry: current frontiers and perspectives in pathology research and practice. *Lab Invest* **95**, 422–431 (2015).
- Do, T. D. et al. Optically guided single cell mass spectrometry of rat dorsal root ganglia to profile lipids, peptides and proteins. *ChemPhysChem* **19**, 1180–1191 (2018).
- Burnette, W. N. “Western Blotting”: electrophoretic transfer of proteins from sodium dodecyl sulfate-polyacrylamide gels to unmodified nitrocellulose and radiographic detection with antibody and radioiodinated protein A. *Anal. Biochem.* **112**, 195–203 (1981).
- Towbin, H., Staehelin, T. & Gordon, J. Electrophoretic transfer of proteins from polyacrylamide gels to nitrocellulose sheets: procedure and some applications. *Proc. Natl Acad. Sci. USA* **76**, 4350–4354 (1979).
- Jin, S. et al. Multiplexed Western blotting using microchip electrophoresis. *Anal. Chem.* **88**, 6703–6710 (2016).
- Wood, D. K., Weingeist, D. M., Bhatia, S. N. & Engelward, B. P. Single cell trapping and DNA damage analysis using microwell arrays. *Proc. Natl Acad. Sci. USA* **107**, 10008–10013 (2010).
- Hughes, A. J. et al. Single-cell western blotting. *Nat. Methods* **11**, 749–755 (2014).
- Sinkala, E. et al. Profiling protein expression in circulating tumour cells using microfluidic western blotting. *Nat. Commun.* **8**, 14622 (2017).
- Rosàs-Canyelles, E., Dai, T., Li, S. & Herr, A. E. Mouse-to-mouse variation in maturation heterogeneity of smooth muscle cells. *Lab Chip* **18**, 1875–1883 (2018).
- Kang, C.-C. et al. Electrophoretic cytopathology resolves ERBB2 forms with single-cell resolution. *npj Precis. Oncol.* **2**, 10 (2018).
- Yamauchi, K. A. & Herr, A. E. Subcellular western blotting of single cells. *Microsyst. Nanoeng.* **3**, 16079 (2017).
- Tentori, A. M., Yamauchi, K. A. & Herr, A. E. Detection of Isoforms Differing by a Single Charge Unit in Individual Cells. *Angew. Chem.* **128**, 12619–12623 (2016).
- Yamauchi, K. A., Tentori, A. M. & Herr, A. E. Arrayed isoelectric focusing using photopatterned multi-domain hydrogels. *Electrophoresis* **39**, 1040–1047 (2018).
- Zhang, Y., Naguro, I. & Herr, A. E. In situ single-cell Western blot on adherent cell culture. *Angew. Chem. Int. Ed.* **58**, 13929–13934 (2019).
- Lin, J.-M. G. et al. Linking invasive motility to protein expression in single tumor cells. *Lab Chip* **18**, 371–384 (2018).
- Chen, F., Tillberg, P. W., & Boyden, E. S. Expansion Microscopy. *Science* **347**, 543–548 (2015).
- Tomer, R., Ye, L., Hsueh, B. & Deisseroth, K. Advanced CLARITY for rapid and high-resolution imaging of intact tissues. *Nat. Protoc.* **9**, 1682–1697 (2014).
- Burnette, W. N. “Western blotting”: electrophoretic transfer of proteins from sodium dodecyl sulfate-polyacrylamide gels to unmodified nitrocellulose and radiographic detection with antibody and radioiodinated protein A. *Anal. Biochem.* **112**, 195–203 (1981).
- Ventzki, R. & Stegemann, J. High-throughput separation of DNA and proteins by three-dimensional geometry gel electrophoresis: feasibility studies. *Electrophoresis* **24**, 4153–4160 (2003).
- Englert, C. R., Baibakov, G. V. & Emmert-Buck, M. R. Layered expression scanning: rapid molecular profiling of tumor samples advances in brief layered expression scanning: rapid molecular profiling of tumor samples. *Cancer Res.* **60**, 1526–1530 (2000).
- Zhu, L., Tangrea, M. A., Mukherjee, S. & Emmert-Buck, M. R. Layered electrophoretic transfer - a method for pre-analytic processing of histological sections. *Proteomics* **11**, 883–889 (2011).
- Hughes, A. J., Lin, R. K. C., Peehl, D. M. & Herr, A. E. Microfluidic integration for automated targeted proteomic assays. *Proc. Natl Acad. Sci. USA* **109**, 5972–5977 (2012).

46. Ferguson, K. A. Starch-gel electrophoresis—Application to the classification of pituitary proteins and polypeptides. *Metabolism* **13**, 985–1002 (1964).
47. Squire, P. G.; Moser, P. & O’Konski, C. T. The Hydrodynamic Properties of Bovine Serum Albumin Monomer and Dimer. *Biochemistry* **7**, 4261–4272 (1968).
48. Sah, H. Stabilization of proteins against methylene chloride/water interface-induced denaturation and aggregation. *J. Control. Release* **58**, 143–151 (1999).
49. Oliva, A. & Farin, B. Comparative study of protein molecular weights by size-exclusion chromatography and laser-light scattering. *J. Pharm. Biomed. Anal.* **25**, 833–841 (2001).
50. Miller, C. C. The Stokes-Einstein law for diffusion in solution. *Proc. R. Soc. Lond.* **106**, 724–749 (1924).
51. Park, I. H., Johnson, C. S. & Gabriel, D. A. Probe diffusion in polyacrylamide gels as observed by means of holographic relaxation methods: search for a universal equation. *Macromolecules* **23**, 1548–1553 (1990).
52. Vlassakis, J. & Herr, A. E. Joule heating-induced dispersion in open microfluidic electrophoretic cytometry. *Anal. Chem.* **89**, 12787–12796 (2017).
53. Macounová, K., Cabrera, C. R., Holl, M. R. & Yager, P. Generation of natural pH gradients in microfluidic channels for use in isoelectric focusing. *Anal. Chem.* **72**, 3745–3751 (2000).
54. Sarder, P. & Nehorai, A. Deconvolution methods for 3-D fluorescence microscopy images. *IEEE Signal Process. Mag.* **23**, 32–45 (2006).
55. Sibarita, J. B. Deconvolution microscopy. *Adv. Biochem. Eng. Biotechnol.* **95**, 201–243 (2005).
56. McNally, J. G., Karpova, T., Cooper, J. & Conchello, J. A. Three-dimensional imaging by deconvolution microscopy. *Methods* **19**, 373–385 (1999).
57. Pattle, R. E. Diffusion from an instantaneous point source with concentration dependent coefficient. *Quart. J. Mech. Appl. Math.* **12**, 407–409 (1959).
58. Monck, J. R., Oberhauser, A. F., Keating, T. J. & Fernandez, J. M. Thin-section ratiometric Ca²⁺ images obtained by optical sectioning of fura-2 loaded mast cells. *J. Cell Biol.* **116**, 745–759 (1992).
59. Pawley, J. B. *Biological Confocal Microscopy*. (2006).
60. Duplâtre, G., Ferreira Marques, M. F. & Da Graça Miguel, M. Size of sodium dodecyl sulfate micelles in aqueous solutions as studied by positron annihilation lifetime spectroscopy. *J. Phys. Chem.* **100**, 16608–16612 (1996).
61. Stetsenko, A. & Guskov, A. An overview of the top ten detergents used for membrane protein crystallization. *Crystals* **7**, 197 (2017).
62. Tong, J. & Anderson, J. L. Partitioning and diffusion of proteins and linear polymers in polyacrylamide gels. *Biophys. J.* **70**, 1505–1513 (1996).
63. Su, A., Smith, B. E. & Herr, A. E. In situ measurement of thermodynamic partitioning in open hydrogels. *Anal. Chem.* **92**, 875–883 (2019).
64. Rabilloud, T. Solubilization of proteins for electrophoretic analyses. *Electrophoresis* **17**, 813–829 (1996).
65. Ngoka, L. C. M. Sample prep for proteomics of breast cancer: Proteomics and gene ontology reveal dramatic differences in protein solubilization preferences of radioimmunoprecipitation assay and urea lysis buffers. *Proteome Sci.* **6**, 1–24 (2008).
66. Wiśniewski, J. R., Zougman, A., Nagaraj, N. & Mann, M. Universal sample preparation method for proteome analysis. *Nat. Methods* **6**, 359–362 (2009).
67. Glatter, T., Ahrné, E. & Schmidt, A. Comparison of different sample preparation protocols reveals lysis buffer-specific extraction biases in gram-negative bacteria and human cells. *J. Proteome Res.* **14**, 4472–4485 (2015).
68. Kim, J. J., Chan, P. P. Y., Vlassakis, J., Geldert, A. & Herr, A. E. MicroParticle delivery of protein markers for single-cell Western blotting from microwells. *Small* **1802865**, 1–11 (2018).
69. Huisken, J., Swoger, J., Del Bene, F., Wittbrodt, J. & Stelzer, E. H. K. Optical sectioning deep inside live embryos by selective plane illumination microscopy. *Science* **305**, 1007–1009 (2004).
70. Brown, R. B. & Audet, J. Current techniques for single-cell lysis. *J. R. Soc. Interface* **5**, S131–S138 (2008).
71. Luo, S., Feng, J. & Pang, H. M. High-throughput protein analysis by multiplexed sodium dodecyl sulfate capillary gel electrophoresis with UV absorption detection. *J. Chromatogr. A* **1051**, 131–134 (2004).
72. Kang, C.-C. C. et al. Single cell-resolution western blotting. *Nat. Protoc.* **11**, 1508–1530 (2016).
73. Gumuscu, B. & Herr, A. E. Separation-encoded microparticles for single-cell western blotting. *Lab Chip* **20**, 64–73 (2020).
74. Kang, C.-C. C., Lin, J.-M. G. M., Xu, Z., Kumar, S. & Herr, A. E. Single-cell Western blotting after whole-cell imaging to assess cancer chemotherapeutic response. *Anal. Chem.* **86**, 10429–10436 (2014).
75. Schindelin, J. et al. Fiji: an open-source platform for biological-image analysis. *Nat. Methods* **9**, 676–682 (2012).
76. Schneider, C. A., Rasband, W. S. & Eliceiri, K. W. NIH Image to ImageJ: 25 years of image analysis. *Nat. Methods* **9**, 671–675 (2012).
77. Linkert, M. et al. Metadata matters: access to image data in the real world. *J. Cell Biol.* **189**, 777–782 (2010).
78. Crocker, J. C. & Grier, D. G. Methods of digital video microscopy for colloidal studies. *J. Colloid Interface Sci.* **179**, 298–310 (1996).
79. Blair, D. & Dufresne, E. The Matlab Particle Tracking Code Repository. <http://site.physics.georgetown.edu/matlab/> (2008).
80. Wilkins, D. K. et al. Hydrodynamic radii of native and denatured proteins measured by pulse field gradient NMR techniques. *Biochemistry* **38**, 16424–16431 (1999).
81. Ogston, A. G., Preston, B. N. & Wells, J. D. On the transport of compact particles through solutions of chain-polymers. *Proc. R. Soc. Lond.* **333**, 297–316 (1973).
82. Baselga, J., Hernández-Fuentes, I., Masegosa, R. M. & Llorente, M. A. Effect of crosslinker on swelling and thermodynamic properties of polyacrylamide gels. *Polym. J.* **21**, 467–474 (1989).
83. Liu, C. H. et al. Enhanced cell viability and cell adhesion using low conductivity medium for negative dielectrophoretic cell patterning. *Biotechnol. J.* **5**, 1005–1015 (2010).
84. Mourdoukoutas, A. P., Grist, S. M. & Herr, A. E. Rapid electrotransfer probing for improved detection sensitivity in in-gel immunoassays. *Analytical Methods*, **12**, 4638–4648 (2020).

Acknowledgements

This work was funded in part by the National Cancer Institute of the National Institutes of Health, Cancer Moonshot award, Grant Number: 1R33CA225296-01 to A.E.H. and by the Chan Zuckerberg Biohub. S.M.G. gratefully acknowledges the support of a post-doctoral fellowship from the Natural Sciences and Engineering Research Council of Canada (NSERC). A.P.M. gratefully acknowledges support from the National Science Foundation Graduate Research Fellowship Program (NSF GRFP). We sincerely thank Dr. Burcu Gümüşcü Sefünc for her assistance with early proof-of-concept tests. Confocal and light-sheet imaging experiments were conducted at the CRL Molecular Imaging Center at UC Berkeley, supported by the Helen Wills Neuroscience Institute. We acknowledge all members of the Herr Lab at UC Berkeley, as well as Dr. Ben Smith at UC Berkeley and the group of Prof. Mark Pegram at Stanford University, for useful discussions and feedback. We are also grateful to the CRL Molecular Imaging Center staff as well as Kamran Ahmed and Eva Nichols for assistance with light-sheet imaging setup.

Author contributions

S.M.G. and A.E.H. designed the projection electrophoresis assay. S.M.G., A.P.M., and A.E.H. designed experiments. S.M.G. performed projection electrophoretic separations of purified proteins and single cells. S.M.G. and A.P.M. performed electrophoretic probing experiments. S.M.G. designed software and performed data analysis. All authors wrote the manuscript.

Competing interests

APM declares no competing interests. SMG and AEH declare the existence of a potential financial competing interest: SMG and AEH are co-inventors of University of California intellectual property regarding z-directional electrophoresis.

Additional information

Supplementary information is available for this paper at <https://doi.org/10.1038/s41467-020-19738-1>.

Correspondence and requests for materials should be addressed to A.E.H.

Peer review information *Nature Communications* thanks Robert Kennedy and the other, anonymous, reviewer(s) for their contribution to the peer review of this work.

Reprints and permission information is available at <http://www.nature.com/reprints>

Publisher’s note Springer Nature remains neutral with regard to jurisdictional claims in published maps and institutional affiliations.



Open Access This article is licensed under a Creative Commons Attribution 4.0 International License, which permits use, sharing, adaptation, distribution and reproduction in any medium or format, as long as you give appropriate credit to the original author(s) and the source, provide a link to the Creative Commons license, and indicate if changes were made. The images or other third party material in this article are included in the article’s Creative Commons license, unless indicated otherwise in a credit line to the material. If material is not included in the article’s Creative Commons license and your intended use is not permitted by statutory regulation or exceeds the permitted use, you will need to obtain permission directly from the copyright holder. To view a copy of this license, visit <http://creativecommons.org/licenses/by/4.0/>.

© The Author(s) 2020